Zooglider: An autonomous vehicle for optical and acoustic sensing of zooplankton

Mark D. Ohman [ID],[1]* Russ E. Davis [ID],[1] Jeffrey T. Sherman,[1] Kyle R. Grindley,[1] Benjamin M. Whitmore,[1] Catherine F. Nickels [ID],[1] Jeffrey S. Ellen[2]

[1]Scripps Institution of Oceanography, University of California, San Diego, La Jolla, California
[2]Computer Sciences and Engineering, University of California, San Diego, La Jolla, California

Abstract

We present the design and preliminary results from ocean deployments of *Zooglider*, a new autonomous zooplankton-sensing glider. *Zooglider* is a modified *Spray* glider that includes a low-power camera (Zoocam) with telecentric lens and a custom dual frequency Zonar (200 and 1000 kHz). The Zoocam quantifies zooplankton and marine snow as they flow through a defined volume inside a sampling tunnel. Images are acquired on average every 5 cm from a maximum operating depth of ~ 400 m to the sea surface. Biofouling is mitigated using a dual approach: an ultraviolet light-emitting diode and a mechanical wiper. The Zonar permits differentiation of large and small acoustic backscatterers in larger volumes than can be sampled optically. Other sensors include a pumped conductivity, temperature, and depth unit and chlorophyll *a* fluorometer. *Zooglider* enables fully autonomous in situ measurements of mesozooplankton distributions, together with the three-dimensional orientation of organisms and marine snow in relation to other biotic and physical properties of the ocean water column. It is well suited to resolve thin layers and microscale ocean patchiness. Battery capacity supports 50 d of operations. *Zooglider* includes two-way communications via Iridium, permitting near-real–time transmission of data from each dive profile, as well as interactive instrument control from remote locations for adaptive sampling.

Zooplankton are pivotal components of aquatic ecosystems. Spanning unicellular to complex multicellular life, zooplankton constitute key constituents of food webs and are important modulators of biogeochemical cycles. Functioning relatively low in food webs, they are responsive to physical climate forcing and can even serve to amplify climate signals (e.g., Di Lorenzo and Ohman 2013), making them useful sentinels of a changing climate. Some calcifying zooplankton are at risk as ocean acidification intensifies (e.g., Bednaršek et al. 2014). The size and species structure of the zooplankton alter rates and pathways of carbon export from the surface ocean (Steinberg and Landry 2017). Grazing by herbivorous zooplankton regulates phytoplankton growth (Landry et al. 2009), and carnivorous zooplankton can be responsible for top–down regulation of other zooplankton populations and pelagic food web structure (Pershing et al. 2015). Zooplankton are essential prey influencing feeding success and recruitment of a variety of planktivorous fishes, marine mammals, and seabirds.

Traditional methods for sampling zooplankton include diverse nets, pumps, and high-speed towed instruments (e.g., Reid et al. 2003; Wiebe and Benfield 2003) that are useful but often disrupt the very organisms they sample. Delicate fishing tentacles of cnidarians and ctenophores, mucus houses of appendicularians, feeding webs of thecosome pteropods, fine pseudopodia of planktonic Rhizaria, and fragile appendages of planktonic crustaceans are often disrupted or damaged in the sampling process. Moreover, the relatively coarse vertical resolution of most conventional devices makes it difficult to resolve patch structure of the zooplankton, including vertical thin layers (Cowles et al. 1998) that may be sites of elevated prey–predator interactions. Such sampling methods also fail to resolve the three-dimensional orientation and postures of organisms in their natural environment.

In addition to traditional sampling methods, diverse optical imaging and acoustic devices have been developed to improve the space–time resolution of the distribution of zooplankton in the ocean and in lakes. A spectrum of in situ optical

*Correspondence: mohman@ucsd.edu

Additional Supporting Information may be found in the online version of this article.

imaging systems is available (Davis et al. 1992; Samson et al. 2001; Benfield et al. 2003; Herman et al. 2004; Madin et al. 2006; Cowen and Guigland 2008; Picheral et al. 2010; Schulz et al. 2010; Thompson et al. 2012; Briseño-Avena et al. 2015). Holographic imaging has been implemented (Katz et al. 1999; Watson 2004; Sun et al. 2008). Diverse echo-sounders, including multifrequency active acoustics, are regularly used (e.g., Wiebe et al. 2002) and some instruments integrate both optical imaging and acoustic backscatter (e.g., Jaffe et al. 1998; Briseño-Avena et al. 2015).

These instruments represent a number of important technological advances. But, a common characteristic of virtually all of the above devices is their relatively large size and high power consumption, hence suitability for deployment primarily as towed or profiling instruments from research vessels, moorings, or short-duration autonomous underwater vehicles (AUVs) with extensive battery power. As currently configured, most such instruments are not amenable to small, extended duration, autonomous vehicles such as gliders and floats (but see Checkley et al. 2008). There is need for zooplankton-sensing or measurement devices that can be operated fully autonomously (cf. Perry and Rudnick 2003) and can sustain in situ measurements for extended periods of time.

In response to this need, here we present the development and field tests of *Zooglider*, an autonomous vehicle intended to sense mesozooplankton both optically and acoustically. We sought to develop a navigable underwater vehicle for extended duration (i.e., > 30 d) missions to depths of at least 400 m, with two-way communications permitting on-the-fly changes of instrument characteristics in response to near-real–time measurements, for adaptive sensing. The vehicle should be easily transported and deployed or recovered from small craft. It must generate minimal hydrodynamic and optical disturbance to the surrounding water to minimize avoidance responses of zooplankton. Many additional constraints are imposed that are not faced when building traditional ship-board sampling equipment or AUVs, including the need for low power, small mass, and small volume instruments.

Our imaging system had the further design consideration that it be optimized for mesozooplankton ranging in size from approximately 0.5–20 mm. The volume in which organisms are imaged needs to be maximized (subject to other constraints), and this volume must be well-defined so that quantitative measurement of organism concentrations is possible. Biofouling of optical surfaces needs to be mitigated. For the echo sounders, further considerations are that they be capable of withstanding repeated pressure cycling from the surface to at least 400 m and include at least two acoustic frequencies that can be used to differentiate the contributions of small and large acoustic scatterers to the backscatter signal. The vehicle payload also must accommodate ancillary environmental sensors, including a pumped conductivity, temperature, and depth (CTD) unit and chlorophyll *a* (Chl *a*) fluorometer, as well as standard global positioning system (GPS) and Iridium satellite communications. *Zooglider*, presented here, satisfies all of these requirements.

Below we discuss standard *Spray* features and the design and construction of the Zoocam and Zonar that led to *Zooglider*. We describe our solutions to biofouling, using both an ultraviolet light-emitting diode (UV-LED) and mechanical wiper, and present and evaluate preliminary results from *Zooglider* field deployments.

Materials and procedures

Overall *Zooglider* design

Zooglider is based on the *Spray* glider, designed and built by the Instrument Development Group (IDG), Scripps Institution of Oceanography (Sherman et al. 2002; Davis et al. 2008). *Spray* is 2.0 m long, 0.20 m in diameter, with a wing span of 1.2 m. It uses a hydraulic pump to transfer oil between an internal reservoir and external bladders to change its overall volume and alternate its buoyancy from negative to positive. Internal batteries move to adjust the center of mass and hence pitch and roll. Pitch controls lift on the wings and thus forward motion. Roll induces lateral lift that causes turning. Together, pitch and roll control the flight path, glide angle, and heading. When *Spray* reaches the surface, it rolls the wings vertically putting an embedded antenna at the wingtip above water to acquire a GPS location and transmit its position plus scientific data via Iridium satellite. It also receives new commands from shore, adjusting its dive depth, course, and sampling characteristics. *Spray* is powered by 13 MJ of primary lithium batteries and operates to 1000 m depth. The standard sensor suite includes a custom version of a pumped SeaBird CP41 CTD and a Seapoint mini-scf Chl *a* fluorometer. Safety features include a secondary ARGOS transmitter in case Iridium fails and a drop weight that is released by a "burn wire" in the events (a) pressure exceeds an operating limit or (b) pressure has remained above the surface value longer than a time limit.

The principal modifications to *Spray* in building *Zooglider* (Fig. 1) were the addition of an optical imaging system for zooplankton and marine snow (the Zoocam) and a dual frequency (200 and 1000 kHz) sonar system (the Zonar). Two devices were engineered to mitigate optical biofouling: an UV-LED and a custom mechanical wiper system. In air, *Zooglider* weighs 58.8 kg, including 5.0 kg for the Zoocam and 2.4 kg for the Zonar. Both the Zoocam and Zonar are close to neutrally buoyant in seawater.

Zoocam sampling tunnel and pressure housing

The Zoocam uses shadowgraph imaging to record silhouettes of organisms and marine snow that interrupt the light path as they flow through a sampling tunnel. The leading edge of the sampling tunnel was carefully designed to minimize hydrodynamic disturbances and escape responses by zooplankton, based on shear thresholds found to induce escape responses by planktonic organisms (Haury et al. 1980;

Fields and Yen 1997; Suchman and Sullivan 2000; van Duren et al. 2003; Gilbert and Buskey 2005; Bradley et al. 2013). Flow dynamic modeling (Solidworks Flow Simulation) was employed to analyze different geometric configurations and angles of attack of the leading edge of the flow tunnel, in order to minimize the shear associated with the tunnel in simulated flows of 25 cm s^{-1}. These flow simulations were also used to determine the optimal position of the Zoocam with respect to the nose of the *Spray* glider. The configuration in Figs. 1–2 illustrates the tunnel shape and configuration arrived at following these numerical experiments. The Zoocam

Fig. 1. Rendering of the *Zooglider*, illustrating the Zoocam on the nose and dual-frequency Zonar in the payload bay near the tail. The orange region indicates the pressure case; the contents of the yellow region (payload bay) are exposed to ambient hydrostatic pressure.

pressure housing, pressure-tested to 500 dBar, consists of two parallel pods (Fig. 2). One houses red and UV-LEDs and associated lens and window while the other houses the second window, lens, camera board, and Gumstix Overo controller running a limited version of the Linux operating system. The illuminated light path between the two pods is recessed 11.1 cm from the leading edge of the sampling tunnel.

Camera and illumination

We initially considered light field (Plenoptics) imaging systems because of their three-dimensional resolving capability but determined that the power requirement and image file size were both too large for our objective of extended mission capability. After experimenting with different camera boards, lenses, and illumination systems, we arrived at the following configuration (Fig. 2). Illumination is provided by an LED centered at 620–630 nm (Cree XP-E2). Red light was selected in order to minimize avoidance behavior, as copepod photoreceptors are relatively insensitive to red wavelengths (Stearns and Forward 1984; Buskey et al. 1989; Cohen and Forward 2002). The light is collimated via a 125 mm FL plano-convex, 12.5 mm diameter lens, then reflected by a 45° mirror before passing through a 4.95-cm-diameter sapphire window (10 mm thick by 54 mm diameter) and across the sampling tunnel (Fig. 2b). The seawater optical path length between the two pod windows (where the zooplankton flow) is 15.0 cm. The collimated light passes through the other pod's sapphire window, is reflected by a 45° mirror, then passes through another plano-convex lens, focusing the image on the plane of the camera. This geometry achieves a telecentric lens, for which the size of the imaged object is, in principle, not dependent on its location in the optical path. The camera is the FLIR Chameleon, using the Sony ICX445 CCD with global shutter.
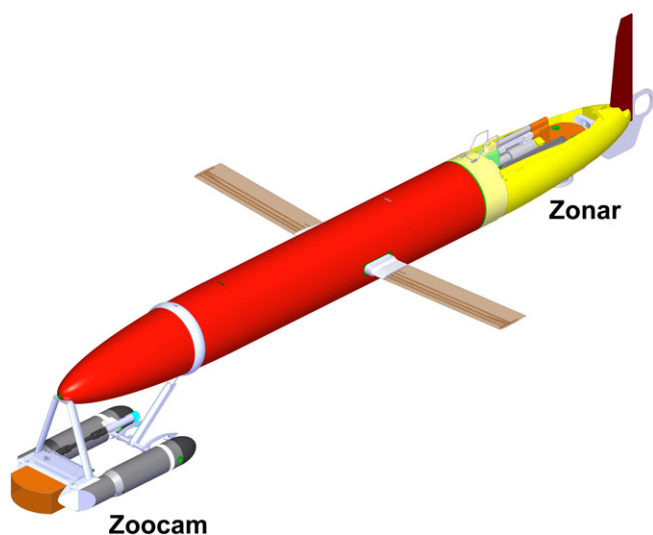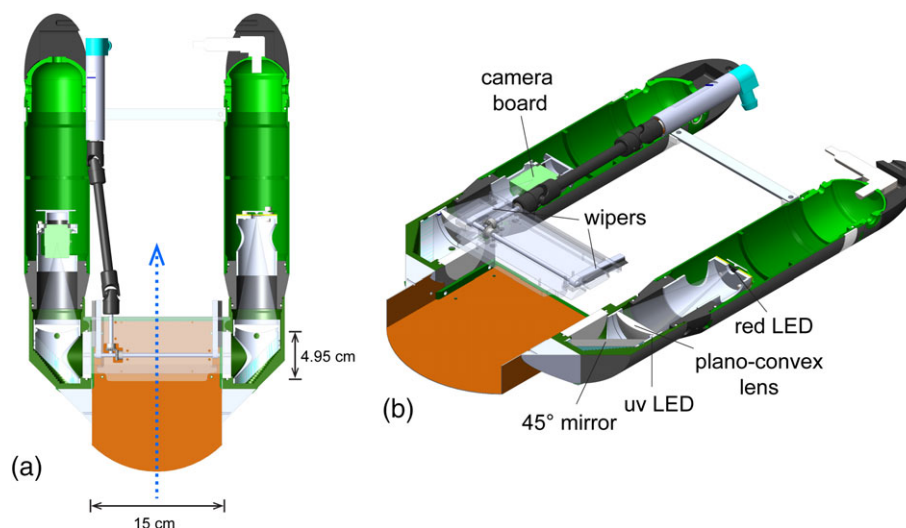

Fig. 2. Zoocam. Water flows unimpeded through the sampling tunnel (dotted line). Right pod houses the light source (red LED), plano-convex lens, UV-LED, and mirror. Left pod houses the plano-convex lens, mirror, camera board, and Gumstix controller. Dark gray shaft powers the wipers. **(a)** Plan view, with partial cutaway. **(b)** Oblique view, cutaway showing lower half.

The image size is 1.2 megapixels (1296 × 964) with a pixel resolution of 40 μm. Although the board supports 12 bit pixels, we acquire at 8 bits to reduce file size and increase the image transfer rate. The red LED illumination is powered continuously during ascent. The camera shutter is triggered at a frequency of 2 Hz with an exposure time of 30–94 μs, and image frames are saved at a rate of 0–2 Hz (software selectable remotely).

Although the diameter of the optical field is 4.95 cm and optical path length is 15.0 cm, the camera's frame does not include the upper and lower edges of the window perimeter, resulting in a total imaged volume of 250 mL per frame. *Zooglider* ascends at an average pitch angle of 16–18° off the horizontal, with a vertical velocity averaging 10 cm s^{-1}. With the Zoocam frame rate at 2 Hz, an image is acquired on average every 5 cm of vertical displacement. Each frame images an independent volume of water.

Data handling and telemetry

The workflow associated with processing Zoocam images is presented in Fig. 3. During *Zooglider's* ascent, the raw Zoocam images are packed into a simple data structure and written to files (10 images per file). Due to the volume of data, low bandwidth, and cost of Iridium, images are not transmitted at sea. Rather, simple size statistics are calculated for the regions of interest (ROIs) and transmitted for each profile. During descent, the 10-image files are processed for ROI statistics, and files are permanently stored to either a 512 Gb universal serial bus thumbdrive or a 200 Gb solid-state drive memory card, yielding > 700 Gb optical data storage per mission at the present time. For simplicity and speed, the real-time ROI detection/sizing algorithm is a one-dimensional model, processed for each vertical pixel column of the image. Each pixel is compared to a threshold value. If the intensity is below that threshold, the light is assumed to be blocked by a particle. For this one-column slice, the "size" of a particle is the length of consecutively blocked pixels. A histogram of the size distribution is collected, with two size categories transmitted real time ("small" where 10 < size < 25 pixels, and "large" where size > 50 pixels). The threshold value is calculated from every 100th image by calculating the pixel distribution per column and setting the threshold to the 7th percentile.

Postrecovery image processing

Upon recovery of *Zooglider*, all frames are downloaded and processed on a server (Fig. 3). The raw images are rewritten as .PNG files. Environmental data (CTD and Chl-*a* fluorescence) and engineering data (including pitch and roll measured by the glider) are recorded in situ at 8 s intervals; then, in post-processing, these data are interpolated to the time of each image frame and embedded within the .PNG image files as .XMP metadata (ISO 2012). Each frame is corrected for uneven illumination by "flat-fielding" (Fig. 4a,b; Shaw 1978; Leach et al. 1980; Ellen 2018; details in Supporting Information).
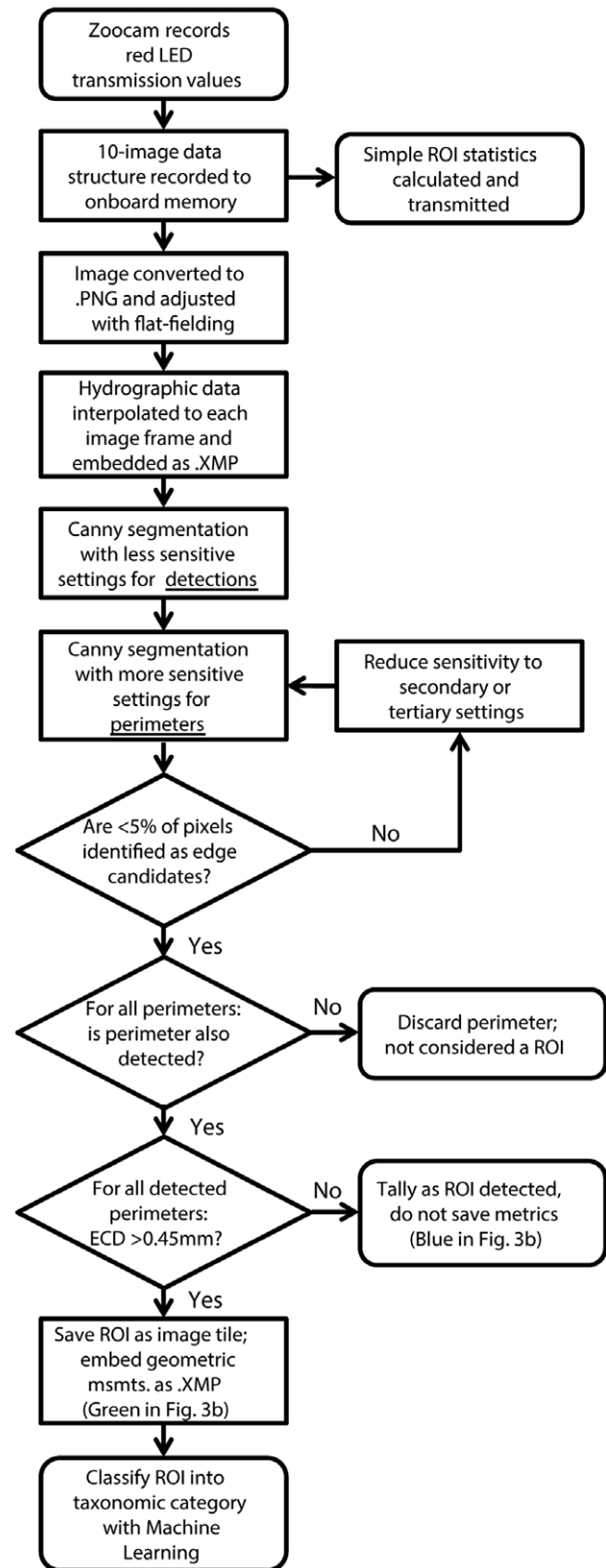

Fig. 3. Flow chart indicating the sequence of steps used in processing Zoocam images.
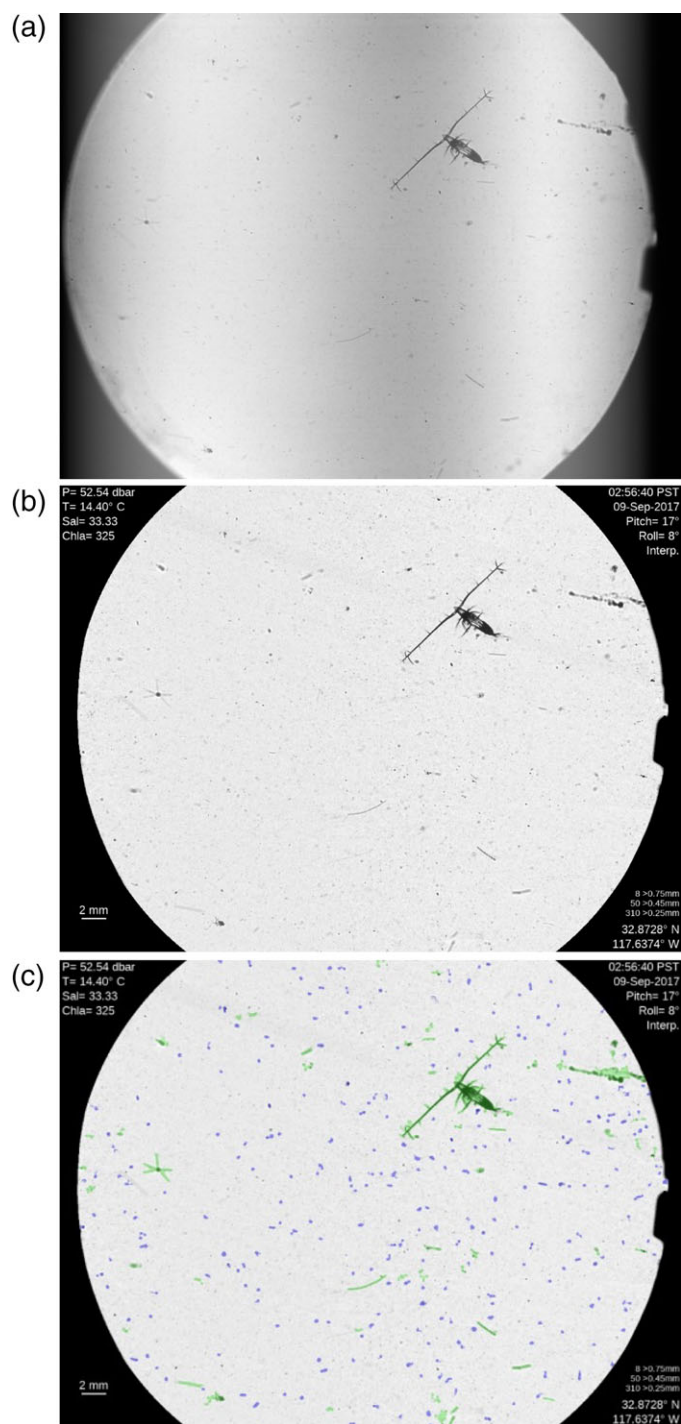
Fig. 4. (a) Raw Zoocam frame. **(b)** Frame after flat-fielding. **(c)** Flat-fielded frame highlighting segmented ROIs detected by dual-pass Canny filter. Green = ROIs > 0.45 mm ECD that are cropped and saved. Blue = ROIs between 0.25 and 0.45 mm ECD that are counted and sized but not saved.

Attempts to standardize backgrounds using histogram normalization, per image normalization, per pixel normalization, and dehazing all generated unsatisfactory results, leading to the methods we describe here (Ellen 2018). After flat-fielding and

contrast enhancement, individual ROIs are identified and segmented using two passes of a Canny edge detector (Fig. 4c; Canny 1986; details in Supporting Information). The first pass is used as a detector. On the second pass, more sensitive thresholds are used to define segmentation boundaries. We merge all edges into contiguous regions and create a binary mask of objects/nonobjects for both versions of Canny. We retain as a ROI all objects that are greater than 100 pixels in area (equivalent to ~ 0.45 mm, Equivalent Circular Diameter (ECD)) and are detected by both versions of our Canny implementation, which eliminates weak/false positive ROIs. We segment the ROI only according to the boundaries recognized by the second pass. We then take approximately 70 measurements (ROI area, convex perimeter, angular orientation, equivalent circular diameter, feret diameter, fractal dimension, major and minor axis length of an ellipse, grayscale distribution, etc.). We add a scalebar and a 30 pixel wide frame and save the ROI with the measurements embedded as metadata in .XMP format. ROIs < 30 pixels in area (0.25 mm ECD) are discarded; ROIs between 30 and 100 pixels (0.25–0.45 mm ECD) are counted and sized but not saved; ROIs > 100 pixels (0.45 mm ECD) are counted, sized, and saved.

When the concentration of marine snow particles in the full frame is too dense, the optimal segmentation algorithm returns the entire frame as a single ROI. Therefore, when the number of raw edge pixels exceeds 5% of the image, we use a less sensitive threshold and resegment. If the number of edge pixels still exceeds 5%, a tertiary sensitivity threshold is used. This procedure results in a more accurate ROI count by avoiding an object count of 1 for a dense field of small objects at the cost of some accuracy defining the perimeter of individual ROIs. Bi et al. (2015) also found multiple passes and thresholds to be useful for plankton segmentation in turbid waters, using a different baseline algorithm.

Segmented ROIs are initially classified into taxonomic categories using Convolutional Neural Networks (Krizhevsky et al. 2012; LeCun et al. 2015; Luo et al. 2018) then all classifications are manually validated. We will separately report in detail the machine learning approaches we have implemented (J. S. Ellen unpubl.).

Biofouling

Two different sources of biofouling were addressed: (1) growth of bacteria and other microorganisms on optical windows, together with settlement of propagules of multicellular organisms, and (2) entanglement of tentacles, salp chains, and other pieces of organisms across the optical window. To address (1), we incorporated an UV-LED light source behind the optical window, pointed toward the window opposite (Fig. 2b). As sapphire absorbs relatively little UV light, one LED served to irradiate both optical windows. We used the Crystal IS UVC 20-250-280 nm LED, operated at 100 mA input current, delivering a hypothetical 20 mW of output power in the 250–280 nm band. The UV-LED is activated only
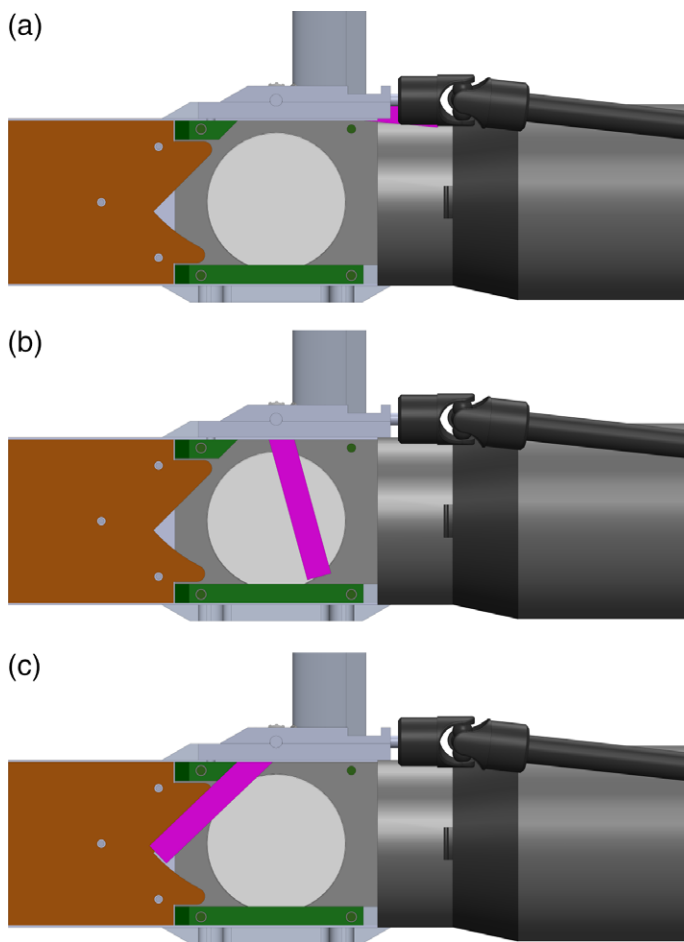
Fig. 5. Internal view of one side of the sampling tunnel indicating operation of the wipers (highlighted in magenta). **(a)** Wiper retracted out of the light path and flow tunnel. **(b)** Wiper partially extended over the optical window. **(c)** Wiper at full extent.

on *Zooglider* descent when the red illumination and camera are powered off. The UV-LED is then turned off at a programmable depth during descent, chosen so that the UV-LED is on for 25% of a full dive cycle. To address (2), i.e., entanglement of occasional snagged tentacles and other organic matter, we added custom mechanical wipers. The wipers use a mechanical linkage system from a microcontrolled Direct Current (DC) brushless motor to a rubber wiper blade at each window. The pressure-compensated (oil-filled) motor rotates the wipers back-and-forth through a 135° arc (Fig. 5). At the start of each descent, *Zooglider* turns on the UV-LED and activates the wiper's microcontroller. The surfaces of both optical windows are wiped three times near the sea surface. Between uses, the wipers retract into the "up" position behind the top crossplate where they do not interfere with the flow through the sampling tunnel (Figs. 2b, 5). The gear assembly that drives the wipers is housed in a low-profile assembly situated atop the sampling tunnel (Fig. 5). This assembly has a faired leading edge and is recessed 9.1 cm from the forward edge of the tunnel, minimizing disturbances to the flow.
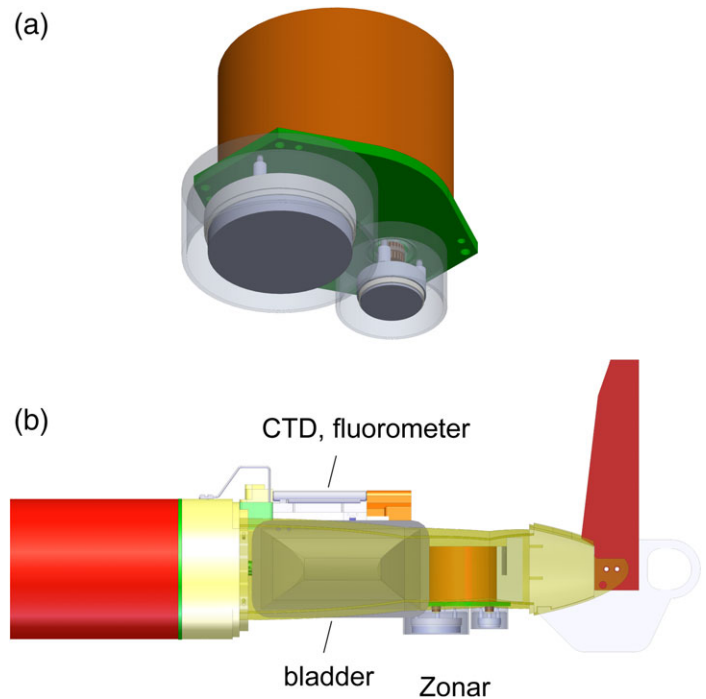

Fig. 6. (a) Dual-frequency Zonar (200/1000 kHz) in housing. **(b)** Zonar mounted in the posterior portion of the *Zooglider* payload bay (side of bay is removed for clarity).

Zonar

The Zonar consists of single-beam 200 and 1000 kHz transducers manufactured by the IDG (Fig. 6; details in Supporting Information). The piston diameter of the 200 kHz transducer is 42 mm, yielding a half power (−6 dB) full beam angle of 10°. The diameter of the 1 MHz transducer is 22 mm, yielding a half power full beam angle of 4°. Both transducers use a 6 ms pulse length and 5 kHz sampling rate. The 200 kHz scans returns for 60 ms and the 1 MHz scans for 50 ms. The time between pings is 200 ms for the 200 kHz and 100 ms for the 1 MHz. To avoid transducer ringing and near-field effects, a blanking time is set to 1 ms. Every 4 m on ascent, a four-ping burst ensemble is transmitted on the 200 kHz beam, then on the 1 MHz. These both sample approximately the same water parcel in depth, but due to the wider beam, the 200 kHz samples a larger volume. Due to this difference in volume, direct ping-to-ping variance between the two frequencies is not statistically valid. Depth and time averaging is required to produce statistically meaningful comparisons of size distributions.

The transmitted pulse is reflected by particles (mainly zooplankton) that affect the return signal strength, $E(R)$ (dB), as a function of range, R. At great range, there is no reflection, and $E(R)$ is a measurement of the overall noise of the system, N (dB) (Watkins and Brierley 1996; DeRobertis and Higginbottom 2007). We estimated noise as the average of the minimum $E(R)$ between 20 and 40 m from the transducer at a *Zooglider* depth between 100 and 400 m. This method agreed within 2 dB with the $E(R)$ in listening mode, with no signal

transmitted, when both measures were available for comparison. N was subtracted linearly from $E(R)$. The signal-to-noise ratio (SNR), is SNR = $E(R)_{-N}/N$. Here, we only consider data where SNR(R) > 10 dB.

The return energy $E(R)$ is converted into scattering volume (S_v) using the sonar equation:

$$Sv = E(R) - N - SL - 10\log_{10}\left(c\frac{\tau}{2}\right) - \Psi + 20\log_{10}(R) + 2\alpha R \quad (1)$$

where SL is the source level (dB, determined empirically during calibration), c is the speed of sound in seawater (m s^{-1}), τ is the pulse length (s), Ψ is the equivalent beam angle (dB), α is the absorption loss (dB m^{-1}), and R is the range from the transducer (m; Parker-Stetter et al. 2009). The absorption loss is 0.054 dB m^{-1} for 200 kHz and 0.38 dB m^{-1} for 1 MHz, as calculated using the Ainslie and McColm (1998) algorithm for water properties typical at 100 m depth in the San Diego Trough (10°C, 34.0 Practical Salinity Units (PSU)).

Calibration was performed in a 12 m × 5 m × 3.6 m seawater pool using a 10 mm tungsten carbide sphere target (glued to 0.1 mm nylon monofilament) located 5 m from the transducer face. The transmission pulse was reduced to 0.6 ms to avoid multipath interference. Signal strength was recorded as the transducer was rotated through ± 7° (using a Vernier accurate to 0.25°). This was repeated with the target suspended at different vertical depths (9 cm spacing, equivalent to 1° beam pattern resolution). Calibration yielded an estimate of the beam width, plus a maximum return signal strength, $E(R)$ (dB), for the 10 mm sphere. Noise was estimated as $E(R)$ with transmission off and linearly subtracted from $E(R)$ to produce $E(R)_{-N}$. Anderson (1950) was used to estimate the theoretical target strength (Ts, reflectivity as a function of frequency). The SL was then estimated from the Zonar's measured maximum signal strength (presumed to be on axis) using:

$$SL = E(R)_{-N} + 20\log_{10}R + 2\alpha R - Ts - gain \quad (2)$$

where gain is the instrument gain setting. For each deployment, the in situ noise minus the calibration noise was subtracted from the gain to correct for baseline variation.

Every 4 m on ascent, a four-ping burst ensemble is collected, averaged across pings, corrected for spreading and sound absorption (Eq. 1), and averaged into 1 m depth bins. The 1 m bins are averaged across ensembles, producing a composite $S_v(z)$ spanning the full dive depth. For this study, only bins at a range of 3.0–8.1 m from the Zonar and with SNR > 10 dB were used, corresponding to an ensonified volume of 15.45 m^3 at 200 kHz and 2.57 m^3 at 1 MHz. Details of the conversion from Zonar range to depth may be found in Supporting Information.

If the zooplankton backscatter is approximated by a simple fluid-sphere scattering model (Anderson 1950; Greenlaw 1979;

Johnson 1977), where the sphere's characteristics are a density ratio g = 1.016 and sound speed ratio h = 1.033, then the calculated backscatter intensity ratio for (1000 kHz/200 kHz) for a 0.9 mm equivalent spherical radius is 5 dB. We used this difference to coarsely classify the backscattering by size (Eq. 3), assigning a difference of 5 dB or less ($S_{v\text{-}1000kHz} - S_{v\text{-}200kHz}$) to "large" scatterers, and greater than 5 dB to "small" scatterers.

$$dB\ difference = S_{v\ 1000\ kHz} - S_{v\ 200\ kHz} \quad (3)$$

Only depth bins where both frequencies have a SNR greater than 10 dB are included in the dB differencing.

During ascent, the Zonar is oriented 17° from the vertical axis due to the glider pitch and as much as ± 20° in the cross axis due to roll movements for steering. For targets with random orientation, the Zonar's orientation will not affect acoustic backscatter. However, for targets that do not have spherical scattering and align themselves in a specific orientation with respect to gravity, the Zonar's off axis will have a bias in the backscattered strength.

Fluorometer calibration

In vivo fluorescence recorded by a SeaPoint mini-SCF fluorometer is calibrated against extracts of pure Chl *a*. Fluorescence is also measured for a natural suspension of phytoplankton in seawater collected from the Scripps pier before dawn and maintained in darkness to avoid nonphotochemical quenching. Ninety percent acetone extracts of pure Chl *a* (Sigma-Aldrich C6144-1MG) are analyzed in glass cuvettes in a custom housing at a fixed distance from the light source, permitting responses of different fluorometers (which are consistently linear) to be expressed in the same standardized fluorescence units (SFU; Powell and Ohman 2015). This procedure allows measurement of any changes in fluorometer response before and after a *Zooglider* mission. Immersion of the fluorometer in a natural seawater sample permits assessment of the approximate correspondence between SFU and Chl *a* concentration. An aliquot of pier seawater is separately filtered onto a glass–fiber filter and analyzed on a Turner 10 AU fluorometer with acidification, to measure the absolute concentration of Chl *a*. Following this procedure, for the Chl *a* fluorescence data reported here, 400 digital counts are approximately equivalent to 1 μg Chl *a* L^{-1}, and the fluorometer response is linear.

CTD calibration

SeaBird CP41 CTDs are calibrated by the manufacturer. IDG periodically performs single-point comparisons to an independently calibrated CTD to verify accuracy.

Assessment

Deployment protocol

Zooglider is readily deployed by two people from a small craft (e.g., 6 m length) or larger vessel, typically in water that is at least 75 m deep. After visual confirmation that *Zooglider*

correctly changes buoyancy, sinks, and ascends properly, it is navigated remotely via Iridium to the desired study site or ocean feature. Upon completion of a mission, *Zooglider* is navigated back to a nearshore location for recovery. All instruments are rated to at least 500 m and our usual operating depths are from 0 to 400 m. *Zooglider* moves vertically at ~ 10 cm s^{-1} at a pitch angle of 16–18° off the horizontal, and moves horizontally at ~ 15 cm s^{-1}. Due to extra drag from the Zoocam, *Zooglider* is ~ 1/3 slower than a standard *Spray*. In a typical mission, *Zooglider* makes several dives navigating toward the study destination with the Zoocam sampling at a low rate (e.g., 0.25–0.5 Hz). When the target area is reached, we remotely increase the image rate to 2 Hz. Science data are not collected during descent. *Zooglider* uses the descent time for image processing, and the UV-LED and wipers are operated as indicated above. Upon attaining the desired pressure, the hydraulic pump is activated to increase buoyancy and science sensors are powered on. CTD and fluorometer readings, together with engineering data, are recorded every 8 s on ascent. The Zoocam records images at the prescribed rate (typically 2.0 Hz) as soon as the red LED and camera are powered.

Zooglider can be directed to cycle between the surface and depth with minimal delays, to drift at depth for specified intervals, to ascend at prescribed times, or other scenarios. Science data transmitted after each dive include CTD, Chl *a* fluoresence, Zoocam ROI counts for the defined size bins, Zonar backscatter, and engineering data. Altered waypoints, dive, and sampling specifications can then be sent to *Zooglider*.

In situ imaging

Zoocam images are adequate for detection of ROIs larger than 0.45 mm ECD (e.g., Fig. 7). Figure 7a illustrates a carnivorous copepod (*Euchaeta* sp.) in proximity to four much smaller copepods that are potential prey. Shadowgraph imaging permits measuring distance between ROIs in the *x-y* dimension but not in the *z* dimension (which extends 15 cm); hence, the three-dimensional vector distance among ROIs cannot be resolved. However, because the two-dimensional relationship of ROIs to one another is often informative, such as in the apparent incipient predator–prey interaction in Fig. 7a, we chose to store full-image frames rather than to perform onboard image segmentation and save only identified ROIs (which would have decreased image storage requirements). Occasionally, organisms are recorded that span the entire optical frame (49.5 mm in diameter; e.g., Fig. 7b). Fine structures, such as the secondary tentilla that branch off the primary tentacles of this undescribed cydippid ctenophore with entrapped copepod prey, are often visible.

When ROIs are oriented broadside to the image plane, size measurements are relatively accurate. Laboratory trials with a reference object moved through the 15 cm optical depth of the Zoocam while maintaining orthogonal orientation suggested that the length of the object varies by < 11% across this range. This variability is in part attributable to small loss of resolution and therefore less distinct edge boundaries with distance from the mid-point of the optical field and in part to an imperfect collimated beam. However, if ROIs are oriented obliquely to the image plane, rather than orthogonal to it, recorded sizes can be much smaller than the true dimensions. Laboratory trials in a test tank with individual copepods, chaetognaths, euphausiid calyptopes, and hydromedusae suggest that organisms can appear to be as little as 1/3 their true length when oriented obliquely to the image plane. Hence, all reported measurements should be considered minimal values, often underestimating true dimensions.

Our optical imaging volume (250 mL per frame) can lead to image saturation when layers of relatively high concentrations of suspended particulate matter are encountered. For example, on one glider mission to date, *Zooglider* transited a phytoplankton layer greater than 8 μg Chl *a* L^{-1} with high densities of elongate diatom chains and other large particles, resulting in difficulties segmenting individual ROIs. For such high particle load situations, we implemented the alternative ROI detection threshold described in the Materials and Procedures section.

Representative Zoocam images of other multicellular zooplankton (Fig. 8) reveal details of copepod setae, tentacles of hydromedusae and siphonophores, ctenophore cilia, appendicularian houses, and internal structure of salps and doliolids. Larger protists, especially those bearing tests of biogenic silica (phaeodarians and collodarians), strontium sulfate (acantharians), and calcium carbonate (foraminfera) are often well resolved (Fig. 9). Delicate spines and pseudopods are often detected. All ROIs are shown in their natural orientation as recorded in situ, except that each ROI should be rotated 16–18° (the average pitch of *Zooglider*) to the right in order to rectify vertical to the top of the image.

In addition to living organisms, the Zoocam resolves detrital material across a range of sizes. Marine snow is often defined as particulate organic matter > 0.5 mm (e.g., Alldredge 1998), a size threshold that corresponds to the minimum size ROI that we segment and save. Most of our Zoocam images are of marine snow, which can vary greatly in morphological characteristics. Small detritus and larger marine snow can vary substantially even within a single dive profile. Figure 10c,d illustrate that Zoocam frames separated vertically by 21 m can show large differences in form. On this dive, at 66.25 dBar, the detritus is small (< 0.5 mm) and nearly spherical, while at 87.64 dBar, the snow is dominated by elongate, streaky clumps that are 2–4 mm in length. It is noteworthy that the vertical maximum of ROI counts (Fig. 10b, which is dominated by detrital particles), was located considerably deeper than the Chl *a* fluorescence maximum (Fig. 10a) in this location. Marine snow imaged on different dives and depths show diverse shapes, constituent particles, and opacity (Fig. 10e). On occasion, zooplankton are found in association with the snow particles.
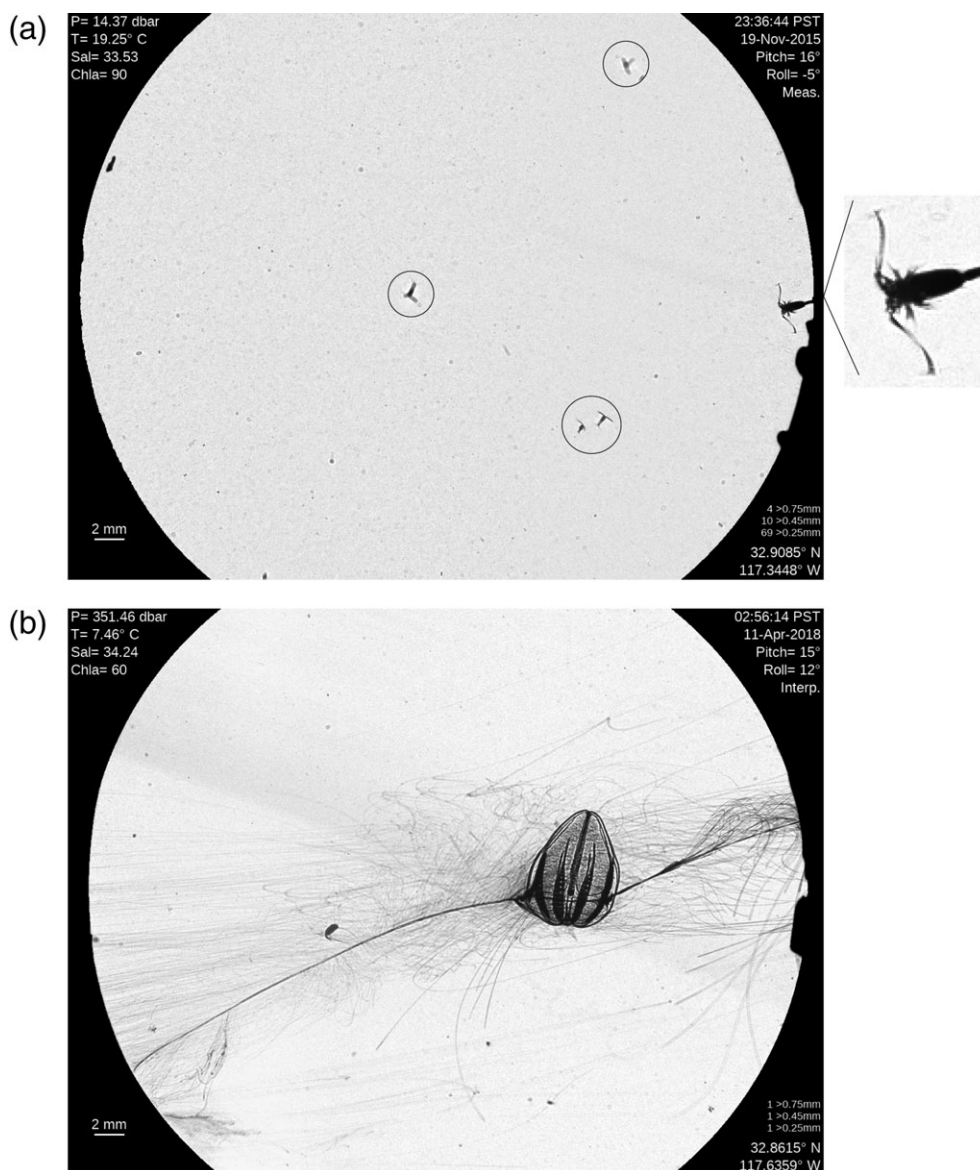
Fig. 7. Zoocam frames imaged in situ. **(a)** Predatory copepod (*Euchaeta*, enlarged to the right) and four small prey copepods (14.37 dBar, 23:36:44, 19 November 2015). **(b)** Undescribed cydippid ctenophore with copepod snared in tentilla (351.46 dBar, 02:56:14, 11 April 2018).

Example deployments

Another illustration of the benefits of *Zooglider* is the markedly enhanced vertical resolution that is possible relative to conventional shipboard sampling with nets or pumps. Figure 11 shows daytime vertical profiles of copepods and appendicularians near the San Diego Trough on 12 March 2017. Both taxa are found in layers as thin as 1–3 m, with concentrations far above the mean. The maximum concentration of copepods in this profile is 76 individuals per liter and that of appendicularians is 20 per liter, local concentrations that greatly exceed the values previously determined in this region by net and pump sampling. Such elevated local densities can markedly increase expected rates of prey–predator encounter and attack (Yen 1985). It is also noteworthy that the layer of

maximum concentration of copepods is offset vertically far from the depth of the Chl *a* maximum layer. The vertical profile of appendicularians illustrates that one population mode partially overlaps the upper region of the Chl *a* maximum, but another mode of highest concentrations of appendicularians is found in relatively narrow depth intervals located much shallower in the water column (Fig. 11d).

Another *Zooglider* mission is illustrated in Fig. 12. *Zooglider* was deployed west of the Scripps pier, then navigated remotely to a location over the San Diego Trough in ~ 950 m of water (5–14 September 2017, SDT2). The Zoocam frame rate was 2.0 Hz continuously. The deep Chl *a* maximum layer was well-defined at 40–50 m depth (Fig. 12b). Densities of smaller (0.45–1.0 mm ECD) ROIs recorded by the Zoocam were also
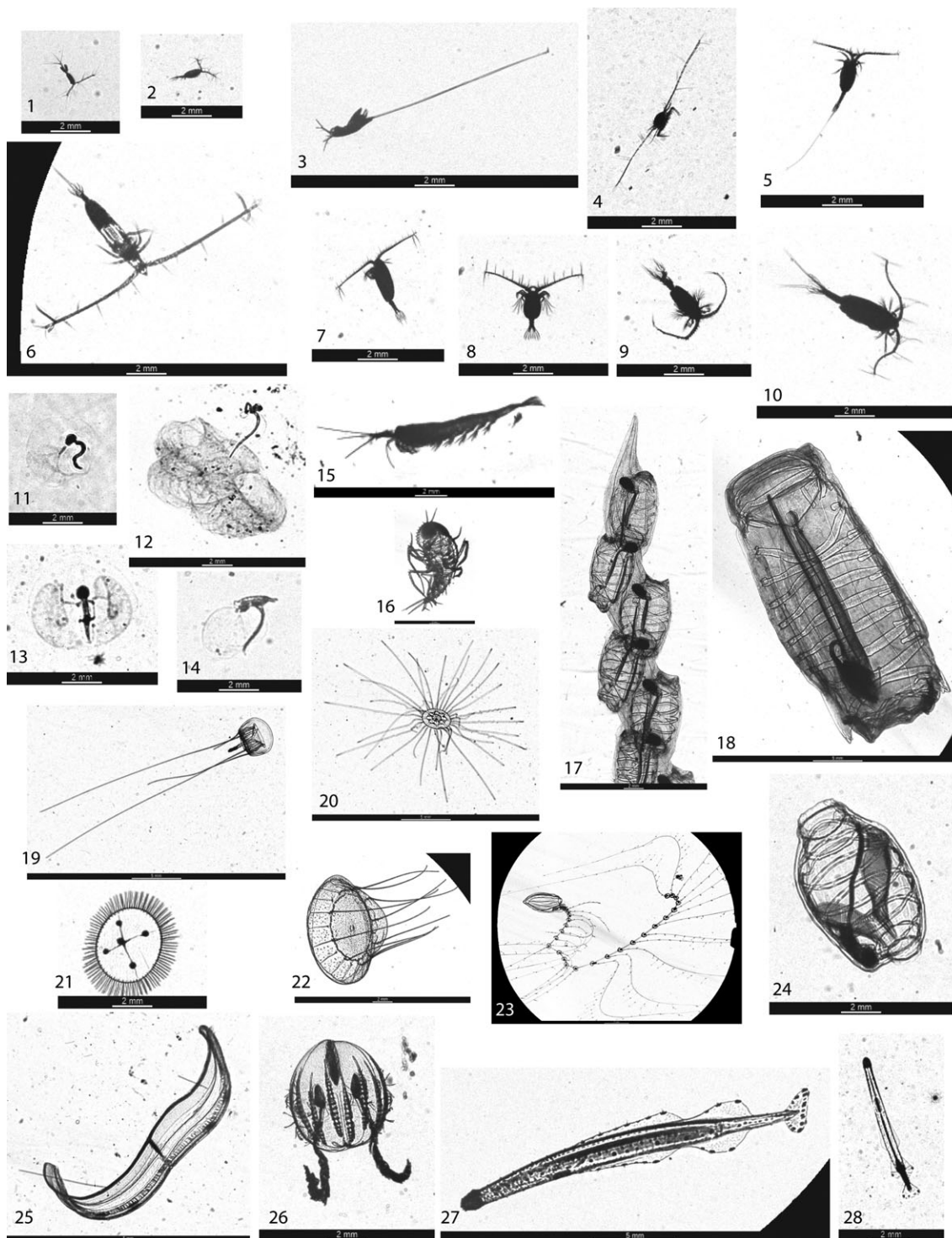
Fig. 8. Multicellular zooplankton imaged in situ by the Zoocam. **(1–10)** Copepods (1, *Oithona*; 2, calanoid; 3, *Aegisthus*; 4, calanoid; 5, *Heterorhabdus*?; 6, *Eucalanus californicus*; 7, *Calanus pacificus*; 8, *Euchirella*; 9, *Pleuromamma*; 10, *Euchaeta*), **(11–14)** appendicularians (11, *Oikopleura*; 14, *Fritillaria*), **(15)** euphausiid (*Nyctiphanes simplex*?), **(16)** hyperiid amphipod, **(17, 18)** salps (*Salpa fusiformis*; 17, aggregate; 18, solitary), **(19–22)** medusae (19, unknown; 20, trachymedusa; 21, *Obelia*; 22, narcomedusa), **(23)** siphonophore (*Lensia*), **(24)** doliolid (*Dolioletta gegenbauri*), **(25, 26)** ctenophores (25, *Velamen parallelum*; 26, *Pleurobrachia bachei*), and **(27, 28)** chaetognaths. All organisms are shown in their natural orientation, except that each ROI should be rotated 16–18° (the pitch of *Zooglider*) to the right to rectify 0° straight up. Note scale bars beneath each organism.
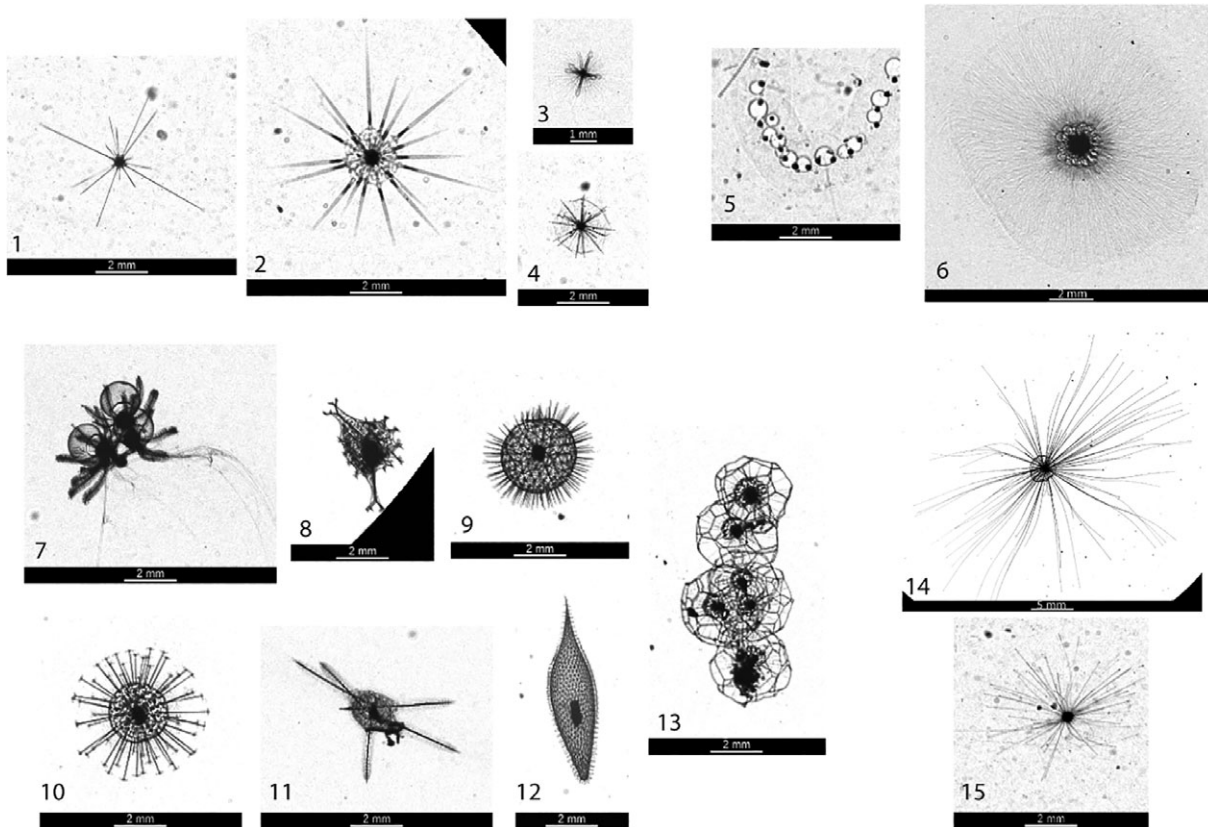
Fig. 9. Unicelluar (protistan) zooplankton imaged in situ by the Zoocam. **(1–4)** Acantharia, **(5, 6)** Collodaria, **(7–13)** Phaeodaria (7, Medusettidae; 8, Coelodendridae [*Coelographis*? morph. 3]; 9, Aulosphaeridae; 10, unknown; 11, Coelodendridae [*Coelographis*? morph. 1]; 12, Coelodendridae [*Coelographis*? morph. 2]; 13, Cannosphaeridae), **(14, 15)** foraminifera (14, hastigerinid). All organisms are shown in their natural orientation, except that each ROI should be rotated 16–18° (the pitch of *Zooglider*) to the right to rectify 0° straight up. Note scale bars beneath each organism.

elevated in this layer during *Zooglider* profiles over the San Diego Trough (dives 12–64), while a secondary shallow ROI layer was seen near 30 m in the initial outbound dives and closer to the surface (0–15 m) in the final inbound dives (Fig. 12c). White vertical bands indicate depths where the Zoocam did not record. Larger (> 2.0 mm ECD) ROIs were primarily concentrated in the upper 50 m (Fig. 12d). Occasional vertical bands (Fig. 12d) indicate a ROI (siphonophore tentacle or salp chain) that remained on the Zoocam on ascent across multiple depths. A somewhat lower resolution version (vertical bins ~ 2 to 3 m) of these ROI distribution plots is available in near-real time, permitting directed response of *Zooglider* to features of interest in the water column.

Zonar volume backscatter at 200 kHz from SDT2 shows evidence of a reproducible diel vertical migration (DVM), with a mode ascending from depths of 350–280 m by day to 80–30 m by night (Fig. 12f). $S_{v\text{-200kHz}}$ is elevated at depth by day and at 80–30 m by night ($p < 0.001$; Mann–Whitney U-test). Zonar volume backscatter at 1000 kHz, which includes both smaller and larger organisms, also records this DVM signal (Fig. 12e), although with more broadly dispersed layers. The advantage of dB differencing of the two acoustic frequencies is that it permits us to separate the behavior of the smaller from the larger

acoustic backscatters. Accordingly, by day between 280 and 230 m and at night in the uppermost layer between 30 and 0 m, $S_{v\text{-1000kHz - 200kHz}}$ is dominated by smaller backscatters (i.e., dB difference > 5; teal shading in Fig. 12g). Backscatter attributable to smaller organisms is significantly stronger between 30 and 0 m at night than by day ($p < 0.001$, Mann–Whitney U-test). In contrast, the slightly deeper (80–30 m) nighttime layer is dominated by larger backscatterers (i.e., dB difference < 5; yellow and red shading in Fig. 12g). Thus, there is a size dependence of DVM, with larger backscatterers migrating from ~ 320 to 50 m and smaller backscatters migrating vertically from ~ 250 m (and other depths) into the upper 50 m. While such size-dependent DVM is not unexpected (cf. Ohman and Romagnan 2016), it can be detected here in near-real time on an autonomous platform without the use of a research vessel. (Note that the size categories in Fig. 12c,d cannot be directly compared with those in Fig. 12e,f,g, because the wavelengths of sound used on the Zonar [1.5 and 7.5 mm for 1000 and 200 kHz, respectively] are not the same as the selected optical size categories.)

Our intent is not to fully analyze all details of these *Zooglider* missions here but to illustrate some of *Zooglider*'s instrumental capabilities. The bioacoustic information shown in
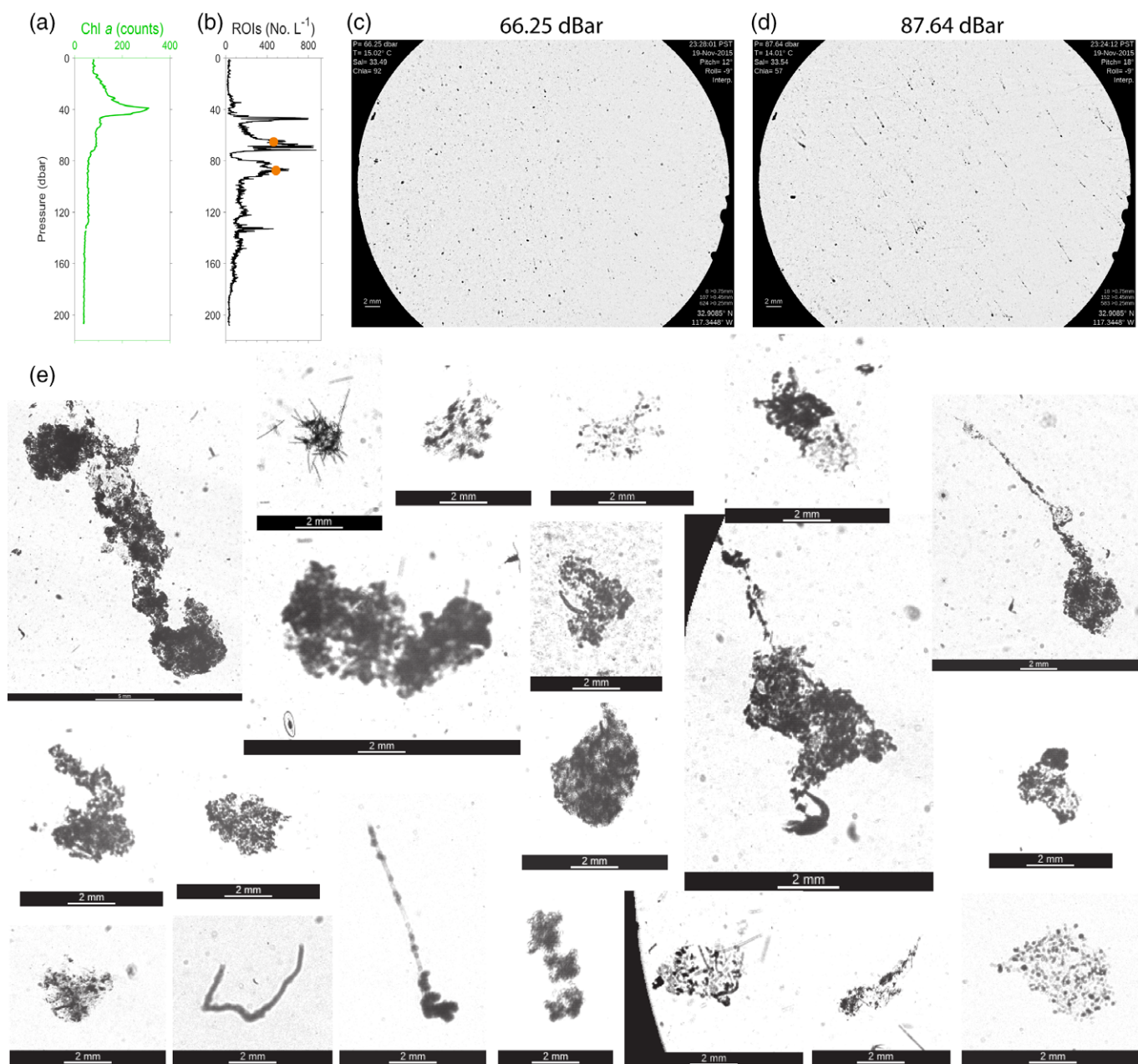
Fig. 10. Marine snow imaged in situ by the Zoocam. **(a)** Vertical profile of Chl *a* fluorescence (digital counts), between 23:02 and 23:40 h, 19 November 2015, Scripps Canyon. **(b)** Vertical profile of ROIs L^{-1} (total > 0.45 mm ECD). Orange dots indicate the depths of the two Zoocam frames displayed to the right. **(c)** Zoocam frame from 66.25 dBar; **(d)** Zoocam frame from 87.64 dBar. **(e)** Diverse marine snow morphologies from different depths and *Zooglider* missions. All particles are shown in their natural orientation, except that each ROI should be rotated 16–18° (the pitch of *Zooglider*) to the right to rectify 0° straight up. Note scale bars beneath each ROI.

Fig. 12e–g is available in near-real time (albeit at somewhat lower vertical resolution) and can also be used adaptively to target specific layers or other features of interest.

Discussion

The fully autonomous *Zooglider* is suitable for in situ imaging of a spectrum of different types of mesozooplankton, including both multicellular organisms and larger heterotrophic protists, as well as marine snow. Imaging is done in a well-circumscribed sampling volume, making it possible to quantify densities of organisms and particles. The dual frequency Zonar permits distinction of smaller and larger acoustic backscatterers, with much larger sampling volumes than is possible with optical imaging. *Zooglider* accomplishes this with a vehicle that is readily deployed, controlled, and recovered, using two-way remote communications and navigation.
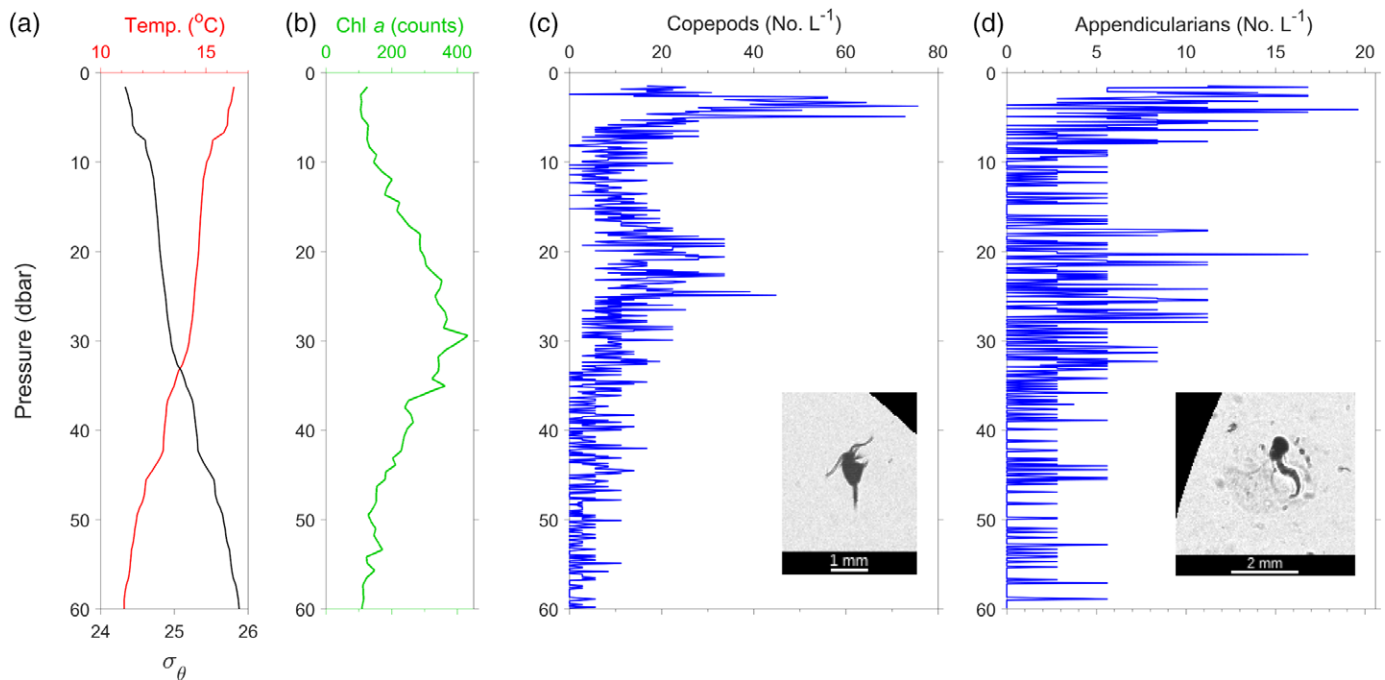
Fig. 11. *Zooglider* profiles near the San Diego Trough, 13:21–13:31 h, (Zooglider Rendezvous, ZGRV, 12 March 2017). Vertical profiles of **(a)** temperature (°C) and density (σ_θ), **(b)** Chl *a* fluorescence (digital counts), **(c)** copepod density (No. L^{-1}), and **(d)** appendicularian density (No. L^{-1}). Profiles in **(c)** and **(d)** are based on Zoocam images.

Shadowgraph imaging (e.g., Benfield et al. 2003; Cowen and Guigland 2008) and active bioacoustics at more than one frequency (e.g., Holliday et al. 1989; Wiebe and Benfield 2003; DeRobertis et al. 2010) are known technologies, but here we incorporate them for the first time in an endurance glider. The novel aspects of *Zooglider* are development of a low-power zooplankton-tuned camera and sonars and their incorporation into an autonomous vertically profiling vehicle with near-real–time data reporting and two-way communications for remote instrument control. Unlike drifting floats (e.g., DeRobertis and Ohman 1999; Checkley et al. 2008), *Zooglider* can be navigated over hundreds of kilometers to locations and features of interest and back again. This permits acquisition of large volumes of data at much lower cost and higher vertical resolution than previously possible.

This autonomous capability opens new possibilities for resolving ocean phenomena when research vessels cannot be present, towed vehicles are disruptive, or geographically fixed sensors on moorings are not appropriate. Dynamic features such as ocean fronts (Belkin et al. 2009) that can markedly restructure plankton communities (e.g., Landry et al. 2012; Powell and Ohman 2015) and alter C export (Stukel et al. 2017) are amenable to investigation. Responses to event-scale perturbations, such as upwelling–downwelling, wind-mixing, or predator passage (Nickels et al. 2018) events can be quantified. Quasi-Lagrangian studies that entail repeated measurements of the zooplankton over time are feasible. Vertical thin layers of zooplankton and marine snow (e.g., Cowles

et al. 1998; Alldredge et al. 2002) can now be resolved by our autonomous vehicle at scales as small as 5 cm, which is the scale at which interactions between predators and prey, grazers and algae, detritivores and snow, and mate-finding all occur.

Zooglider appears to be minimally invasive. We have detected little evidence for avoidance responses by the targeted organisms, although this topic awaits quantitative assessment. Work-in-progress will evaluate the taxonomic and size composition of zooplankton sensed by *Zooglider* in relation to independent net samples, but here we note that imaged organisms rarely demonstrate escape postures. Notably, this is true for planktonic copepods, which have refined sensory capabilities and rapid escape responses (e.g., Buskey et al. 2002). Euphausiids, which can have excellent avoidance responses (e.g., Brinton 1967), are detected and imaged by the Zoocam. Indirect evidence that flow through the Zoocam sampling tunnel does not perturb most animals includes the outstretched, delicate tentacles and apparently natural feeding postures of cnidarians and ctenophores. Appendicularians are frequently found in their houses. Chaetognaths are usually in an elongate position, and copepods typically have outstretched first antennae. Foraminifera display pseudopodia extending far from their tests. Marine snow appears to be imaged without disrupting its structure.

The Zoocam records the vertical orientation of animals (and marine snow) in situ. This capability opens the door to investigations of natural swimming and foraging postures
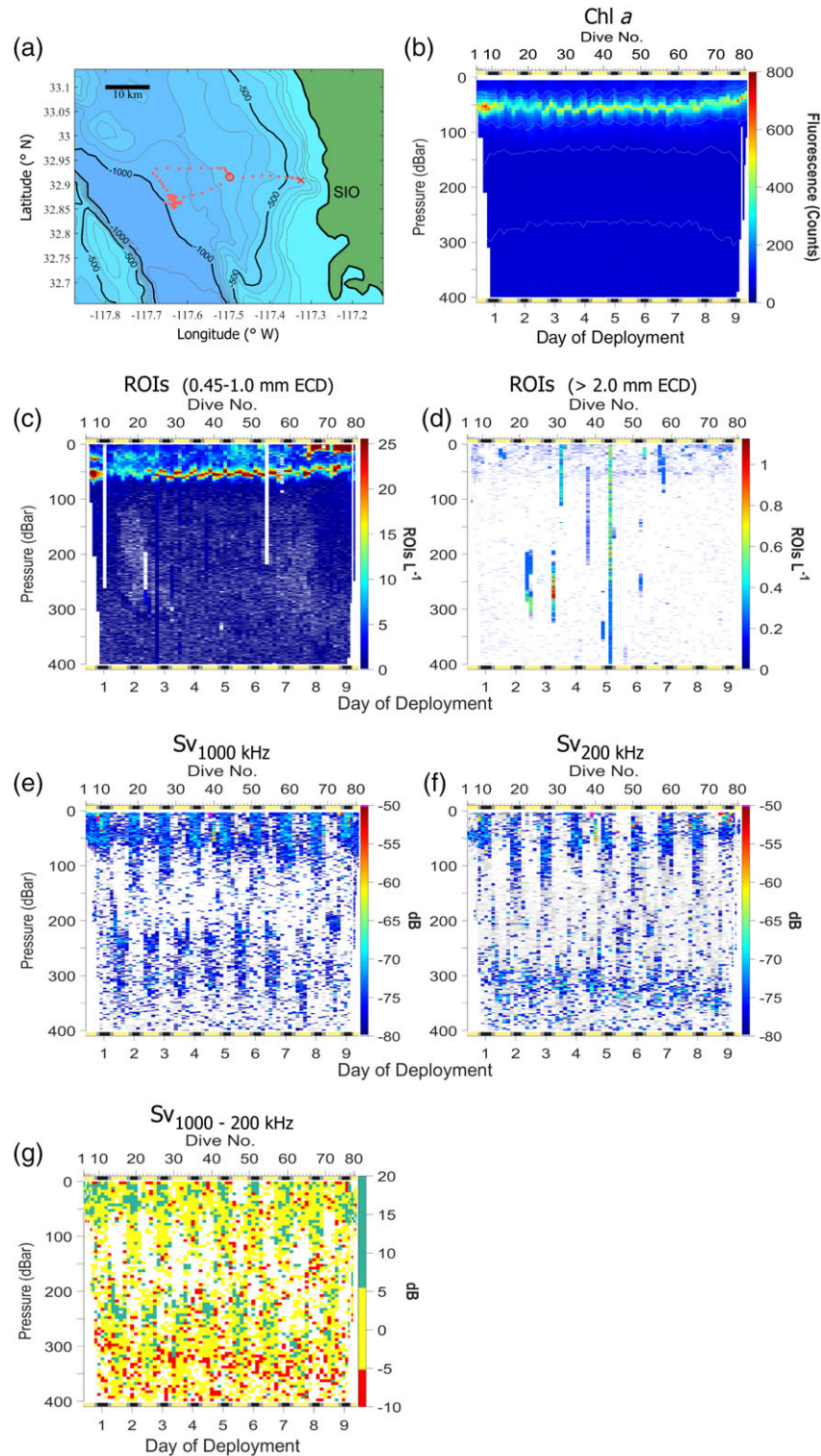
Fig. 12. *Zooglider* mission over the San Diego Trough (SDT2, 5–14 September 2017). **(a)** Red dots indicate dive locations, and X indicates recovery location. Depth contours in meters. **(b)** Chl *a* fluorescence (colors) superimposed on density (σ_θ) contours (white lines). **(c)** ROI counts (No. L^{-1}) between 0.45 and 1.0 mm ECD; **(d)** ROI counts (No. L^{-1}) > 2.0 mm ECD. **(e)** Volume backscatter (S_v, dB) at 1000 kHz (gray < −80 dB). **(f)** Volume backscatter (S_v, dB) at 200 kHz (gray < −80 dB). **(g)** dB-differenced volume backscatter ($S_{v\ 1000kHz} - S_{v\ 200kHz}$).

(e.g., D. E. Gaskell et al. unpubl.) and how these and other behavioral characteristics vary with respect to depth and in response to environmental stimuli.

Another advantage of *Zooglider* as an instrument platform is that its sensors are untethered to a surface vessel and thus not influenced by vibrations or ship heave transmitted to depth. Such motions can also be a drawback in mooring deployments. Surface research vessels also emit light pollution that can alter nocturnal zooplankton behavior (Ludvigsen et al. 2018). Because our sensors emit only UV or red light (enclosed inside a sampling tunnel, set back from its leading edge), there should be only minimal optical disturbance of the surrounding water. The blue light of the fluorometer is fully contained in a flow-through housing and located 2 m away the Zoocam. For acoustic sensing, it is advantageous to have transducers carried subsurface by the vehicle, as we do here, rather than ensonifying the water column from a bottom-deployed, upward-looking, or surface-deployed, downward-looking instrument. In the latter case, the acoustic energy must penetrate a surface layer perturbed by bubble entrainment along the hull of research vessels as well as by wind mixing. Unlike surface- or bottom-deployed echo sounders, the target detection probability of the Zonar is constant with depth, because the transducers are at the same range from acoustic targets at all depths transited.

Silhouette imaging is well suited to the nearly transparent organisms found in the plankton (see also Cowen and Guigland 2008), but it should be noted that the optical density of the silhouettes does not correspond to the organisms' opacity and appearance in situ under reflected light. Furthermore, as noted above, while the size of a ROI does not vary substantially with distance along the collimated light beam, size measurements of ROIs should always be considered a minimum value. The orientation of the long axis of the body relative to the light source can markedly alter the ROI's apparent size.

A drawback to in situ imaging is that the optical resolution and inability to control organism orientation usually make it difficult to arrive at species- or developmental stage-level identifications (but see Hirche et al. 2014). Such information is often essential for studies of population dynamics, biodiversity, and other topics. In addition, physical samples are not acquired, precluding many types of molecular and biogeochemical analyses. The accumulation of large numbers of images means that advanced machine learning methods are required for efficient classification of images. We will report independently on our progress using Deep Learning methods for image classification (J. S. Ellen unpubl.).

Biofouling is of paramount concern for optical devices deployed in the ocean for extended periods. To date, we have found the UV-LED to be very effective at inhibiting growth of organisms on the optical surfaces. A different source of biofouling, i.e., entrapment of elongate cnidarian tentacles or salp chains can be problematic. Our wiper appears to be effective in removing such objects, although we operate the wiper

only just prior to the beginning of a dive, in order to avoid interrupting image acquisition during ascent. If tentacle entrapment contaminates images during a *Zooglider* ascent and the tentacles remain attached, the structures are removed at the end of a dive by the mechanical wiper, thus only a single dive's images are compromised.

Battery power is sufficient to operate *Zooglider* for missions up to 50 d in duration. This is a major distinction from AUVs, which typically operate for short periods of time (often 24–48 h). At present, a limitation on *Zooglider* mission duration is the memory required to store full frame images. Acquiring Zoocam images at the full frame rate of 2 Hz currently permits missions of 10–14 d duration, although duration can readily be extended by lowering the image acquisition rate. We expect memory capabilities will continue to increase in the future.

When the red LED is initially powered on, the average grayscale reading diminishes with time for approximately the first 150–200 s as the light source warms up. Hence, it is necessary to use a time-dependent background and flat-field correction in order to make images comparable across a dive.

The Zoocam and Zonar are not designed to image the same volume of water at the same time. The two devices are oriented in different directions (Zoocam forward and Zonar obliquely downward as *Zooglider* ascends). This reflects a basic limitation of acoustic sensing, where it is necessary to ignore the acoustic return closest to the transducers (Medwin and Clay 1998). The Zonar (a) uses a blanking time of 1 ms and (b) transmits a 6 ms pulse, thus ensonifying a large enough volume to average over many scatterers. The average range of the first scan is 3 m, representing the volume-averaged scattered return ranging 0.75–5.25 m from the Zonar. In contrast, the Zoocam must image zooplankton close to the light source. While a limited number of instruments have successfully colocated optical and acoustically sensed volumes (e.g., Jaffe et al. 1998), this was not our objective. Also, there is a large discrepancy between the volumes of water in which zooplankton are sensed by our two instruments. The Zoocam images 250 mL per frame, typically 5 L m^{-1} traveled vertically, while the Zonar ensonifies a much larger volume of water, > 2.57–15.45 m^3 per ping. Thus, the Zonar is detecting objects in a volume 500–3000 times larger than imaged by the Zoocam, making it far more likely that larger, rarer organisms will be detected acoustically. Hence, we sought to obtain measures of acoustic backscatter and optically identified objects in the same general water parcel as *Zooglider*, without attempting to coregister them within a small part of that volume.

In summary, *Zooglider* is a new instrument to optically image mesozooplankton and marine snow in situ, while simultaneously recording acoustic backscatter at two acoustic frequencies, Chl *a*, temperature, and salinity in the same water parcel. The instrument operates between 0 and 400 m depth and is completely autonomous but with remote two-way communication and directed navigation via satellite. It is an

endurance vehicle, capable of 50 d missions. It provides near-real–time data and is suited to both prescribed sampling trajectories and adaptive feature-based sampling for a broad spectrum of studies addressing the ecological interactions of zooplankton and their importance in ocean biogeochemical cycles.

References

Ainslie, M. A., and J. G. McColm. 1998. A simplified formula for viscous and chemical absorption in sea water. J. Acoust. Soc. Am. **103**: 1671–1672.

Alldredge, A. 1998. The carbon, nitrogen and mass content of marine snow as a function of aggregate size. Deep-Sea Res. **45**: 529–541.

Alldredge, A. L., and others. 2002. Occurrence and mechanisms of formation of a dramatic thin layer of marine snow in a shallow Pacific fjord. Mar. Ecol. Prog. Ser. **233**: 1–12. doi:10.3354/meps233001, 10.3354/meps233001

Anderson, V. C. 1950. Sound scattering from a fluid sphere. J. Acoust. Soc. Am. **22**: 426–431.

Bednaršek, N., and others. 2014. *Limacina helicina* shell dissolution as an indicator of declining habitat suitability owing to ocean acidification in the California Current Ecosystem. Proc. R. Soc. B Biol. Sci. **281**. doi:10.1098/rspb.2014.0123

Belkin, I. M., P. C. Cornillon, and K. Sherman. 2009. Fronts in large marine ecosystems. Prog. Oceanogr. **81**: 223–236. doi:10.1016/j.pocean.2009.04.015

Benfield, M., C. Schwehm, R. Fredericks, G. Squyres, S. Keenan, and M. Trevorrow. 2003. ZOOVIS: A high-resolution digital still camera system for measurement of fine-scale zooplankton distributions. *In* P. Strutton and L. Seuront [eds.], Scales in aquatic ecology: Measurement, analysis and simulation. CRC Press.

Bi, H. S., and others. 2015. A semi-automated image analysis procedure for in situ plankton imaging systems. PLoS One **10**. doi:10.1371/journal.pone.0127121

Bradley, C. J., J. R. Strickler, E. J. Buskey, and P. H. Lenz. 2013. Swimming and escape behavior in two species of calanoid copepods from nauplius to adult. J. Plankton Res. **35**: 49–65. doi:10.1093/plankt/fbs088

Brinton, E. 1967. Vertical migration and avoidance capability of euphausiids in the California Current. Limnol. Oceanogr. **12**: 451–483. doi:10.4319/lo.1967.12.3.0451

Briseño-Avena, C., P. L. D. Roberts, P. J. S. Franks, and J. S. Jaffe. 2015. ZOOPS-O^2: A broadband echosounder with coordinated stereo optical imaging for observing plankton in situ. Methods Oceanogr. **12**: 36–54. doi:10.1016/j.mio.2015.07.001

Buskey, E. J., K. S. Baker, R. C. Smith, and E. Swift. 1989. Photosensitivity of the oceanic copepods *Pleuromamma gracilis* and *Pleuromamma xiphias* and its relationship to light penetration and daytime depth distribution. Mar. Ecol. Prog. Ser. **55**: 207–216. doi:10.3354/meps055207

Buskey, E. J., P. H. Lenz, and D. K. Hartline. 2002. Escape behavior of planktonic copepods in response to hydrodynamic disturbances: High speed video analysis. Mar. Ecol. Prog. Ser. **235**: 135–146. doi:10.3354/meps235135

Canny, J. 1986. A computational approach to edge detection. IEEE Trans. Pattern Anal. Mach. Intell. **8**: 679–698. doi:10.1109/tpami.1986.4767851

Checkley, D. M., Jr., R. E. Davis, A. W. Herman, G. A. Jackson, B. Beanlands, and L. A. Regier. 2008. Assessing plankton and other particles in situ with the SOLOPC. Limnol. Oceanogr. **53**: 2123–2136. doi:10.4319/lo.2008.53.5_part_2.2123

Cohen, J. H., and R. B. Forward. 2002. Spectral sensitivity of vertically migrating marine copepods. Biol. Bull. **203**: 307–314. doi:10.2307/1543573

Cowen, R. K., and C. M. Guigland. 2008. In situ ichthyoplankton imaging system (ISIIS): System design and preliminary results. Limnol. Oceanogr.: Methods. **6**: 126–132. doi:10.4319/lom.2008.6.126

Cowles, T. J., R. A. Desiderio, and M. E. Carr. 1998. Small-scale planktonic structure: Persistence and trophic consequences. Oceanography **11**: 4–9. doi:10.5670/oceanog.1998.08

Davis, C. S., S. M. Gallager, M. S. Berman, L. R. Haury, and J. R. Strickler. 1992. The video plankton recorder (VPR): Design and initial results. Arch. Hydrobiol. Beih. Ergebn. Limnol. **36**: 67–81.

Davis, R. E., M. D. Ohman, D. L. Rudnick, J. T. Sherman, and B. Hodges. 2008. Glider surveillance of physics and biology in the southern California Current System. Limnol. Oceanogr. **53**: 2151–2168. doi:10.4319/lo.2008.53.5_part_2.2151

DeRobertis, A., and M. D. Ohman. 1999. A free-drifting mimic of vertically migrating zooplankton. J. Plankton Res. **21**: 1865–1875. doi:10.1093/plankt/21.10.1865

DeRobertis, A., and I. Higginbottom. 2007. A post-processing technique to estimate the signal-to-noise ratio and remove echosounder background noise. ICES J. Mar. Sci. **64**: 1282–1291. doi:10.1093/icesjms/fsm112

DeRobertis, A., D. R. Mckelvey, and P. H. Ressler. 2010. Development and application of an empirical multifrequency method for backscatter classification. Can. J. Fish. Aquat. Sci. **67**: 1459–1474. doi:10.1139/F10-075

Di Lorenzo, E., and M. D. Ohman. 2013. A double-integration hypothesis to explain ocean ecosystem response to climate forcing. Proc. Natl. Acad. Sci. USA **110**: 2496–2499. doi:10.1073/pnas.1218022110

Ellen, J. S. 2018. Improving biological object classification in plankton images using convolutional neural networks, geometric features, and context metadata. PhD thesis. Computer Science and Engineering, Univ. of California, San Diego.

Fields, D. M., and J. Yen. 1997. Implications of the feeding current structure of *Euchaeta rimana*, a carnivorous pelagic

copepod, on the spatial orientation of their prey. J. Plankton Res. **19**: 79–95. doi:10.1093/plankt/19.1.79

Gilbert, O. M., and E. J. Buskey. 2005. Turbulence decreases the hydrodynamic predator sensing ability of the calanoid copepod *Acartia tonsa*. J. Plankton Res. **27**: 1067–1071. doi: 10.1093/plankt/fbi066

Greenlaw, C. F. 1979. Acoustical estimation of zooplankton populations. Limnol. Oceanogr. **24**: 226–242. doi:10.4319/lo.1979.24.2.0226

Haury, L. R., D. E. Kenyon, and J. R. Brooks. 1980. Experimental evaluation of the avoidance reaction of *Calanus finmarchicus*. J. Plankton Res. **2**: 187–202. doi:10.1093/plankt/2.3.187

Herman, A. W., B. Beanlands, and E. F. Phillips. 2004. The next generation of Optical Plankton Counter: The laser-OPC. J. Plankton Res. **26**: 1135–1145. doi:10.1093/plankt/fbh095

Hirche, H. J., K. Barz, P. Ayon, and J. Schulz. 2014. High resolution vertical distribution of the copepod *Calanus chilensis* in relation to the shallow oxygen minimum zone off northern Peru using LOKI, a new plankton imaging system. Deep-Sea Res. **88**: 63–73. doi:10.1016/j.dsr.2014.03.001

Holliday, D. V., R. E. Pieper, and G. S. Kleppel. 1989. Determination of zooplankton size and distribution with multifrequency acoustic technology. J. Conseil. **46**: 52–61.

ISO. 2012. Graphic technology—extensible metadata platform (XMP) specification—part 1: Data model, serialization and core properties, p. 1–46. International Organization for Standardization. ISO/TC 130 Graphic Technology Technical Committee. doi:10.1111/j.1552-6909.2012.01343.x

Jaffe, J. S., M. D. Ohman, and A. De Robertis. 1998. OASIS in the sea: Measurement of the acoustic reflectivity of zooplankton with concurrent optical imaging. Deep-Sea Res. II Top. Stud. Oceanogr. **45**: 1239–1253. doi:10.1016/S0967-0645(98)00030-7

Johnson, R. K. 1977. Sound scattering from a fluid sphere revisited. J. Acoust. Soc. Am. **61**: 375–377. doi:10.1121/1.381326

Katz, J., P. L. Donaghay, J. Zhang, S. King, and K. Russell. 1999. Submersible holocamera for detection of particle characteristics and motions in the ocean. Deep-Sea Res. **46**: 1455–1481.

Krizhevsky, A., I. Sutskever, and G. E. Hinton. 2012. ImageNet classification with deep convolutional neural networks, p. 1097–1105. *In*, Proceedings of 25th International Conference on Neural Information Processing Systems. Curran Associates, Inc.

Landry, M. R., M. D. Ohman, R. Goericke, M. R. Stukel, and K. Tsyrklevich. 2009. Lagrangian studies of phytoplankton growth and grazing relationships in a coastal upwelling ecosystem off Southern California. Prog. Oceanogr. **83**: 208–216. doi:10.1016/j.pocean.2009.07.026

Landry, M. R., and others. 2012. Pelagic community responses to a deep-water front in the California Current Ecosystem: Overview of the A-front study. J. Plankton Res. **34**: 739–748. doi:10.1093/plankt/fbs025

Leach, R. W., R. E. Schild, H. Gursky, G. M. Madejski, D. A. Schwartz, and T. C. Weekes. 1980. Description,

performance, and calibration of a charge-coupled-device camera. Publ. Astron. Soc. Pac. **92**: 233–245. doi: 10.1086/130654

Lecun, Y., Y. Bengio, and G. Hinton. 2015. Deep learning. Nature **521**: 436–444. doi:10.1038/nature14539

Ludvigsen, M., and others. 2018. Use of an autonomous surface vehicle reveals small-scale diel vertical migrations of zooplankton and susceptibility to light pollution under low solar irradiance. Sci. Adv. **4**. doi:10.1126/sciadv.aap9887

Luo, J. Y., J.-O. Irisson, B. Graham, C. Guigland, A. Sarafraz, C. Mader, and R. K. Cowen. 2018. Automated plankton image analysis using convolutional neural networks. Limnol. Oceanogr.: Methods **16**: 814–827. doi:10.1002/lom3.10285

Madin, L., E. Horgan, S. Gallager, J. Eaton, and A. Girard. 2006. LAPIS: A new imaging tool for macro-zooplankton, p. 5. *In* , Oceans 2006 Conference, v. **1–4**. IEEE. doi: 10.1038/nature05328

Medwin, H., and C. S. Clay. 1998, Fundamentals of acoustical oceanography. Academic Press.

Nickels, C. F., L. M. Sala, and M. D. Ohman. 2018. The morphology of euphausiid mandibles used to assess selective predation by blue whales in the southern sector of the California Current System. J. Crustac. Biol. **38**: 563–573. doi: 10.1093/jcbiol/ruy062

Ohman, M. D., and J. B. Romagnan. 2016. Nonlinear effects of body size and optical attenuation on Diel Vertical Migration by zooplankton. Limnol. Oceanogr. **61**: 765–770. doi: 10.1002/lno.10251

Parker-Stetter, S. L., L. G. Rudstam, P. J. Sullivan, and D. M. Warner. 2009. Standard operating procedures for fisheries acoustic surveys in the Great Lakes Fisheries Commission, ISSN 1090-1051. Great Lakes Fisheries Commission Special Publication 09–01.

Perry, M. J., and D. L. Rudnick. 2003. Observing the ocean with autonomous and Lagrangian platforms and sensors (ALPS): The role of ALPS in sustained ocean observing systems. Oceanography **16**: 31–36. doi:10.5670/oceanog.2003.06

Pershing, A. J., and others. 2015. Evaluating trophic cascades as drivers of regime shifts in different ocean ecosystems. Philos. Trans. R. Soc. B Biol. Sci. **370**. doi:10.1098/rstb.2013.0265

Picheral, M., L. Guidi, L. Stemmann, D. M. Karl, G. Iddaoud, and G. Gorsky. 2010. The Underwater Vision Profiler 5: An advanced instrument for high spatial resolution studies of particle size spectra and zooplankton. Limnol. Oceanogr.: Methods **8**: 462–473. doi:10.4319/lom.2010.8.462

Powell, J. R., and M. D. Ohman. 2015. Covariability of zooplankton gradients with glider-detected density fronts in the Southern California current system. Deep-Sea Res. II Top. Stud. Oceanogr. **112**: 79–90. doi:10.1016/j.dsr2.2014.04.002

Reid, P. C., J. M. Colebrook, and J. B. L. Matthews. 2003. The Continuous Plankton Recorder: Concepts and history, from plankton indicator to undulating recorders. Prog. Oceanogr. **58**: 117–173. doi:10.1016/j.pocean.2003.08.002

Samson, S., T. Hopkins, A. Remsen, L. Langebrake, T. Sutton, and J. Patten. 2001. A system for high-resolution zooplankton imaging. IEEE J. Ocean. Eng. **26**: 671–676. doi:10.1109/48.972110

Schulz, J., and others. 2010. Imaging of plankton specimens with the lightframe on-sight keyspecies investigation (LOKI) system. J. Euro. Opt. Soc. Rapid Publ. **5**. doi:10.2971/jeos.2010.10017s

Shaw, R. 1978. Evaluating efficiency of imaging processes. Rep. Prog. Phys. **41**: 1103–1155. doi:10.1088/0034-4885/41/7/003

Sherman, J., R. E. Davis, W. B. Owens, and J. Valdes. 2002. The autonomous underwater glider "Spray". IEEE J. Ocean. Eng. **26**: 437–446.

Stearns, D. E., and R. B. Forward. 1984. Photosensiitivity of the calanoid copepod *Acartia tonsa*. Mar. Biol. **82**: 85–89. doi:10.1007/bf00392766

Steinberg, D. K., and M. R. Landry. 2017. Zooplankton and the ocean carbon cycle. Annu. Rev. Mar. Sci. **9**: 413–444. doi:10.1146/annurev-marine-010814-015924

Stukel, M. R., and others. 2017. Mesoscale ocean fronts enhance carbon export due to gravitational sinking and subduction. Proc. Natl. Acad. Sci. USA. **114**: 1252–1257. doi:10.1073/pnas.1609435114

Suchman, C. L., and B. K. Sullivan. 2000. Effect of prey size on vulnerability of copepods to predation by the scyphomedusae *Aurelia aurita* and *Cyanea* sp. J. Plankton Res. **22**: 2289–2306. doi:10.1093/plankt/22.12.2289

Sun, H., P. W. Benzie, N. Burns, D. C. Hendry, M. A. Player, and J. Watson. 2008. Underwater digital holography for studies of marine plankton. Philos. Trans. R. Soc. A Math. Phys. Eng. Sci. **366**: 1789–1806. doi:10.1098/rsta.2007.2187

Thompson, C. M., M. P. Hare, and S. M. Gallager. 2012. Semi-automated image analysis for the identification of bivalve larvae from a Cape Cod estuary. Limnol. Oceanogr.: Methods **10**: 538–554. doi:10.4319/lom.2012.10.538

Van Duren, L. A., E. J. Stamhuis, and J. J. Videler. 2003. Copepod feeding currents: Flow patterns, filtration rates and energetics. J. Exp. Biol. **206**: 255–267. doi:10.1242/jeg.00078

Watkins, J. L., and A. S. Brierley. 1996. A post-processing technique to remove background noise from echo integration data. ICES J. Mar. Sci. **53**: 339–344. doi:10.1006/jmsc.1996.0046

Watson, J. 2004. HoloMar: A holographic camera for subsea imaging of plankton. Sea Technol. **45**: 53–55.

Wiebe, P. H., and M. C. Benfield. 2003. From the Hensen net toward four-dimensional biological oceanography. Prog. Oceanogr. **56**: 7–136. doi:10.1016/S0079-6611(02)00140-4

Wiebe, P. H., and others. 2002. BIOMAPER-II: An integrated instrument platform for coupled biological and physical measurements in coastal and oceanic regimes. IEEE J. Ocean. Eng. **27**: 700–716. doi:10.1109/JOE.2002.1040951

Yen, J. 1985. Selective predation by the carnivorous marine copepod *Euchaeta elongata*: Laboratory measurements of predation rates verified by field observations of temporal and spatial feeding patterns. Limnol. Oceanogr. **30**: 577–597. doi:10.4319/lo.1985.30.3.0577

Conflict of Interest

None declared

1 **Supplemental Information for:**

2 Ohman, M.D., R.E. Davis, J.T. Sherman, K.R. Grindley, B.M. Whitmore, C.F. Nickels, J.S.

3 Ellen. 2018. *Zooglider: an autonomous vehicle for optical and acoustic sensing of*

4 *zooplankton*. Limnology and Oceanography: Methods.

5

6 **Flat-fielding of Zoocam Images**

7   The flat field correction begins with a 100 frame rolling average (i.e., the 50 frames

8 before and after an exposure, excepting the first 50 and last 50 images of each dive). The raw

9 pixel values for each frame are then corrected by subtracting the 'flat-field' as follows. We

10 calculate the single mean intensity value across the 100 adjacent images for all pixel locations, a

11 single value between 0 and 255. We then calculate the mean intensity value across the 100

12 adjacent images for each pixel location, calculate the mean of those mean values, and divide

13 each component mean by the singular mean intensity to create a correction factor matrix of

14 values (clipped at a maximum of 1.75), yielding a correction factor matrix the same size as the

15 image frame of values [0-1.75]. We multiply the raw pixel values pointwise by this correction

16 factor matrix and divide the result by the maximum value in the frame to rescale pixel values to

17 [0-1], at which point the contrast is uniform throughout the image. We increase contrast by

18 performing gamma correction of 2.2 and re-center these new pixel values to have a mean

19 intensity of 0.812 (corresponding to greyscale value of 207). Finally, we clip values below 0.0

20 and above 1.0 and convert back to 8-bit values [0, 255].

21

22

23   **Pseudo-code for flat-fielding an image using a rolling average**

24   #Calculate mean of stack of 100 frames, and the global mean

25    $Pix_c[j,k]$ = image_pixels   #Pixels of current frame in the mask

26   PixMean[j,k] = mean(Σ $Pix_i[j,k]$: for i = [c-50,c+50])   #mean of stack of 100 frames

27   PG = mean(PM[j,k])   #Global-mean value over stack

28

29   #Use the clipped mean to adjust the current image

30   CF[j,k] = PG / PM[j,k]   # / is element-wise division

31   if CF[j,k]>1.75: set CF[j,k]=1.75   #clip

32   PixCorr[j,k] = P[j,k] * CF[j,k]   # * is element-wise multiplication

33

34   #Convert pixel values from 8-bit to 0-1 space for gamma correction

35   PCmax = maximum(PC[j,k])

36   PixCorrNorm[j,k] = PC[j,k] / PCmax

37

38   #Now normalized so 0 <= PCN[j,k] <=1, perform gamma correction

39   gamma = 2.2

40   PixCorrGamma[j,k] = PCN[j,k]^gamma,

41

42   #For aesthetics and consistency, re-center distribution so that mean intensity is 207/255. Clip

43   values that are adjusted too far.

44   PixCorrGammaMean = mean (PCG[j,k])

45	PixCorrRecenter[j,k] = PCG[j,k] * 0.812/PCGM	#Sets mean intensity 207/255
46	if PixCorrRecenter[j,k]<0: PCR[j,k]=0	#clip
47	if PixCorrRecenter[j,k]>1: PCR[j,k]=1	#clip
48	PixFlatField[j,k] = PCR[j,k] * 255	#Final pixel value, now flat-fielded

49

Segmentation of Zoocam Images

51   Regions of Interest (ROIs) are segmented using two passes of an edge detector (Canny

52 1986). Our first pass uses less sensitive settings to generate detection regions, where at least

53 some strong edges will be present. Because the perimeters of many of our target ROIs contain

54 portions that are extremely thin or nearly transparent, we perform a second, more sensitive pass

55 to capture these fine-grained details. This second pass is used as the actual segmented perimeter

56 for geometric feature calculation and ROI retention, but only if the first pass also indicates that

57 some portion of the perimeter was part of a strong detection region. We also created unique

58 procedures for high coincidence frames and ROI at the edge of the frame. We use the Python

59 implementation of OpenCV (Bradski and Kaehler 2000) as well as Scipy (Oliphant 2007) and its

60 scikit-image component (van der Walt et al. 2014) because neither implementation alone

61 provided direct access to all parameter values required. All thresholds and kernel values were

62 determined after extensive evaluation of possible values.

63   For our first pass, we blur using 13 pixel wide Gaussian kernel with $\sigma = 1.5$ and calculate

64 directional gradients using the same filter. We then perform Canny segmentation with a low

65 threshold of 8 and a high threshold of 20 (note: Canny 1986 recommended a ratio of 2:1 or 3:1).

66 Following (Canny 1986), we retain all of the highest threshold edges and moderate edges if they

67   are 8-connected to a strong edge (adjacent or diagonal). To merge nearby line segments into

68   continuous perimeters we dilate with a 5x5 structuring element, and since the purpose of the

69   regions is detection we leave them dilated. We then perform flood fill using 4-connected

70   neighbors (adjacent but not diagonal). We retain these detection regions if their area exceeded

71   100 pixels (corresponding to a roughly 30 pixel or larger area before dilation).

72   Our second pass of the Canny filter also uses blurs and calculates gradients using a

73   Gaussian kernel of size 13, but $\sigma = 1.75$. This pass performs thresholding using low and high

74   values of 25 and 35. We again dilate with a 5x5 structuring element, but then erode with the

75   same 5x5 element so that these perimeters closely match the intensity boundaries. We fill as

76   before and discard all regions with an area less than 30 pixels.

77   We then use the first pass as a detector, discarding all second-pass regions that do not

78   overlap with a region from the first pass. If the candidate region has an area < 100 pixels, we

79   count it but do not record the image tile or any geometric statistics. If the candidate region's area

80   is greater than 100 pixels we retain the ROI as an individual PNG image and calculate geometric

81   features (e.g., area, min/mean/max intensity) and embed these as XMP metadata.

82   As quality control we perform a check against coincidence. We found that in frames

83   with a high density of diatoms or marine snow, the entire field of view is returned as a single

84   latticed ROI. So if the second pass returns greater than 5% of the pixels as edges of candidate

85   regions, the edges are discarded and another attempt is made using a low threshold of 38 and a

86   high threshold of 52, with an otherwise identical procedure. If that still yields greater than 5% of

87   the pixels as edges, a tertiary attempt is performed with a low threshold of 50 and a high

88   threshold of 104, and these ROI are retained regardless of the ratio of edges to original frame.

89   The Canny algorithm does not include frame boundaries as edges. Since many objects of

90   interest, including larger ROIs, will be partially out of the frame, we consider all top and bottom

91   pixels to be candidate edges, as well as all the pixels that are eroded when a 3x3 cross is applied

92   to the mask. The mask is the circular boundary of the camera's field of view.

93

94   **Pseudo-code for 2-pass segmenting of images**

95   **<u>First Pass Canny:</u>**

96   # Blur the current frame

97   Pix[j,k] = image_pixels   #Pixels of current frame

98   PixBlur[j,k] = Pix[j,k] * GaussianKernel(13,1.5)

99

100   #calculate the magnitude of the directional gradients

101   #element-wise, e.g. Python's numpy.hypot

102   GradX[j,k], GradY[j,k] = Directional_Gradients(PB[j,k])

103   Mag[j,k] = hypot(GX[j,k], GY[j,k])

104

105   #Bin edges per direction by the low and high thresholds

106   LowThresh = 8, HighThresh = 20

107   PixStrong[j,k], PixWeak[j,k] = edges_per_direction(GX[j,k], GY[j,k], Mag[j,k], LT, HT)

108

109   #Following Canny (1986) keep only edges meeting criteria

110   Edges[j,k] = hysteresis_thresholding(PixStrong[j,k], PixWeak[j,k])

111

112 #Dilate candidates, fill holes, and save as first pass binary mask which will subsequently be used

113 as detections

114 Edges[j,k] =dilate(Edges[j,k], Ones[5,5])   #Ones = 5x5 array of all 1's

115 RegionsFirstPass[j,k] = fill_holes(Edges[j,k])   # RFP is a binary Mask

116 RegionsFirstPass[j,k] = remove_small_objects(RFP[j,k], min=100)

117

118 **<u>Second Pass Canny:</u>**

119 **# Again, Blur the current frame, slightly different blur**

120 PixBlur[j,k] = Pix[j,k] * GaussianKernel(13,1.75)   #where * is convolution

121

122 #calculate the magnitude of the directional gradients

123 #element-wise, e.g. Python's numpy.hypot

124 GradX[j,k], GradY[j,k] = Directional_Gradients(PB[j,k])

125 Mag[j,k] = hypot(GX[j,k], GY[j,k])

126

127 #Bin edges per direction by the low and high thresholds

128 LowThresh = 25, HighThresh = 35

129 PixStrong[j,k], PixWeak[j,k] = edges_per_direction(GX[j,k], GY[j,k], Mag[j,k], LT, HT)

130

131 #Following Canny (1986) keep only edges meeting criteria

132 Edges[j,k] = hysteresis_thresholding(PixStrong[j,k], PixWeak[j,k])

6

```
133

134    #Check to see if secondary or tertiary settings are required

135    If Edges[j,k] > 5% of image: restart second pass with LT= 38; HT = 52

136    If Edges[j,k] > 5% of image again: restart second pass with LT= 50; HT = 104

137

138    #Dilate and Erode candidates, fill holes, and save as second pass

139    #binary mask which will subsequently be used as boundaries

140    Edges[j,k] = dilate( Edges[j,k], Ones[5,5] )          #mask of 5x5 array of all 1's

141    Edges[j,k] = erode( Edges[j,k], Ones[5,5] )           #Erode, unlike 1st pass

142    RegionsSecondPass[j,k] = fill_holes( Edges[j,k] )     # RSP is a binary Mask

143    RegionsSecondPass [j,k] = remove_small_objects( RSP[j,k], min=30 )

144

145    Detection and Segmentation:

146    For region in RSP[j,k]:

147          If region overlaps RFP[j,k]:

148                If region.area > 100:

149                      Calculate geometric features and retain

150          Else if region.area > 30:

151                Increment ROI count and discard

152

153

154
```

155 **Zonar Design**

156   Both the 200 and 1000 kHz systems use the same transmit and receive topology, with

157 specific R, C components and winding ratios chosen to best match the impedance of the acoustic

158 transducers. The transmit circuitry is comprised of a square-wave driver into a transformer with

159 its output driving the transducer. The receive circuitry has a matching transformer to optimize

160 the transducer's impedance to the best impedance for the first-stage SNR. After a second-stage

161 amplifier and ± 10% bandwidth filter, the signal goes to a log amplifier (AD8307), whose output

162 is low-pass filtered before 5 kHz sampling by a 12-bit A/D. The output of the log-amp is linear

163 in log-space: if its input is A $\sin(\omega t)$, then the output voltage is proportional to 20 log10(A). The

164 total gain of the receive circuitry is 54 dB.

165   For calibration, target strength was determined using a standard 10 mm diameter tungsten

166 carbide reference sphere suspended in water 5.0 m from the transducers in a test tank, with the

167 Zonar rotated through 0.5° angles while recording the return strength.

168

169 **Zonar Range to Depth Conversion**

170   Assume a 4-ping burst ensemble occurs with the *Spray* at depth z_g. For a pulse duration,

171 τ, and blanking time, b, for a time t after the end of the blanking time, the volume backscatter

172 geometric center, r, is located at

173      $r(t) = (b + \tau + t\,) \, c/2$

174 where c is the speed of sound. Due to the 17° pitch angle, the absolute depth is

175      $z(t) = z_g + r(t)\sin(73)$.

176   The ensemble's $S_v(z(t))$ is averaged in t such that 1 m depth bins are formed. Since bursts are

177   collected every 4 m, sequential ensemble S_v bins overlap in depth. All overlapping bins with

178   SNR>10 dB are averaged, producing a $S_v(z)$ that spans the full profile depth.

179

180

181   **References**

182   Bradski, G. 2000. The OpenCV Library. Dr. Dobb's Journal of Software Tools, December 2000.

183   article ID 2236121.

184   Canny, J. 1986. A computational approach to edge detection. IEEE Trans. Pattern Anal. Mach.

185   Intell. 8: 679-698 doi 10.1109/tpami.1986.4767851

186   Oliphant, T. E. 2007. Python for scientific computing. Comput. Sci. Engin. 9: 10-20 doi

187   10.1109/mcse.2007.58

188   Van Der Walt, S. and others 2014. scikit-image: image processing in Python. Peerj 2: doi

189   10.7717/peerj.453

190